Cryo-electron tomography sheds light on the elastic nature of the *Trypanosoma brucei* tripartite attachment complex

Irina Bregy[1,2,3], Julika Radecke[4], Akira Noga[5], Hugo van den Hoek[6], Mara Kern[1], Beat Haenni[2], Benjamin D. Engel[6], C. Alistair Siebert[4], Takashi Ishikawa[5,7], Benoît Zuber[2#], Torsten Ochsenreiter[1#]

[#]corresponding author

[1]Institute of Cell Biology, University of Bern, Baltzerstrasse 4, Bern CH-3012, Switzerland;

[2]Institute of Anatomy, University of Bern, Baltzerstrasse 2, Bern CH-3012, Switzerland;

[3]Graduate School for Cellular and Biomedical Sciences, Freiestrasse 1, Bern CH-3012, Switzerland;

[4]Electron Bio-Imaging Centre, Diamond Light Source, Oxfordshire OX11 0DE, Didcot, United Kingdom;

[5]Division of Biology and Chemistry, Paul Scherrer Institute, Forschungsstrasse 111, Villigen CH-5232, Switzerland

[6]Biozentrum, University of Basel, Spitalstrasse 41, Basel CH-4056, Switzerland

[7]Department of Biology, ETH Zurich, Zurich, Switzerland

Corresponding Authors:

Torsten Ochsenreiter, Baltzerstrasse 4, Institute of Cell Biology, University of Bern, Switzerland, torsten.ochsenreiter@unibe.ch

Benoît Zuber, Baltzerstrasse 2, Institute of Anatomy, University of Bern, Switzerland, benoit.zuber@unibe.ch

Keywords

Cryo-electron tomography (cryo-ET), tripartite attachment complex (TAC), molecular spring, mitochondrial genome anchoring, mitochondrial genome segregation, kDNA, *Trypanosoma brucei*

Abstract

In contrast to many eukaryotic organisms, trypanosomes only contain a single mitochondrion per cell. Within that singular mitochondrion, the protist carries a single mitochondrial genome that consists of a complex DNA network, the kinetoplast DNA (kDNA). Segregation of the replicated kDNA is coordinated by the basal body of the cell's single flagellum. The tripartite attachment complex (TAC) forms a physical connection between the proximal end of the basal body and the kDNA. This allows anchoring of the kDNA throughout the cell cycle and couples kDNA segregation with the separation of the basal bodies prior to cell division. Over the past years, several components of the TAC have been identified. To shed light on the structure of the cytoplasmic part of the TAC (known as the exclusion zone), we performed cryo-electron tomography on whole cells. This allowed us to acquire three-dimensional high-resolution images of the exclusion zone *in situ*. We observed that the

1

33   exclusion zone filaments offer great mechanical flexibility for basal body movement. We measured
34   the dimensions of the individual structural elements of the area, as well as the overall orientation
35   and positioning of the basal bodies towards the mitochondrial kDNA pocket. Using a combination of
36   experimental data and modelling, we generated a structural model of the exclusion zone protein
37   p197. Our findings suggest that the majority of p197 consists of a string of spectrin-like repeats. We
38   propose that these structural units provide the architecture of a molecular spring and that they are
39   required in the TAC to withstand the mechanical forces generated through basal body repositioning
40   events during kDNA segregation and motility of the organism.

Introduction

42   The mitochondrion is a hallmark of eukaryotic life and it is responsible for essential processes ranging
43   from catabolic reactions like oxidative phosphorylation, to anabolic processes such as iron-sulfur
44   cluster assembly (Braymer & Lill, 2017; Friedman & Nunnari, 2014). Many mitochondrial genes have
45   been transferred to the nucleus, and thus the encoded proteins are produced in the cytoplasm and
46   imported into the mitochondrion. Some essential genes, however, remain encoded on the
47   mitochondrial genome. Thus, trypanosomes, like most other eukaryotes, depend on the inheritance
48   of an intact mitochondrial genome for their survival.

49   Along with the other members of the Kinetoplastea, trypanosomes possess one single, large
50   mitochondrion per cell (Tyler et al., 2001). The singular nature of the mitochondrion and
51   mitochondrial genome requires to take special care of replicating and segregating that genome
52   correctly, prior to cytokinesis (Schneider & Ochsenreiter, 2018). Because of their unique
53   mitochondrial biology, trypanosomes evolved a distinct mitochondrial DNA structure, with highly
54   adapted replication and segregation proteins.

55   The mitochondrial DNA in trypanosomes is condensed to a disc-like network of interlocked circular
56   DNA molecules that are positioned at the posterior end of the cell body (Jensen & Englund, 2012).
57   This structure has been termed the kinetoplast, with its DNA content referred to as the kinetoplast
58   DNA (kDNA) (Trager, 1965). The kDNA consists of two major classes of DNA molecules. The
59   maxicircles (~25 molecules of ~23 kb) encode for cryptogenes that depend on an mRNA editing
60   process to form translatable mRNAs (Hajduk & Ochsenreiter, 2010; Jensen & Englund, 2012;
61   Povelones, 2014). Editing sites on primary mRNAs are recognized by guide RNAs, which are encoded
62   on the ~5000 minicircles (~1kb) (Hong & Simpson, 2003; Ochsenreiter et al., 2007). With the help of
63   guide RNAs, an enzymatic machinery called the editosome can then insert/delete uridine residues
64   from the primary mRNA to form a modified mRNA that encodes for a translatable open reading
65   frame (ORF). Within the kDNA network, minicircles are interlocked with each other and the
66   maxicircles (Chen et al., 1995). With a thickness of about half the circumference of a minicircle, the
67   kDNA dimensions depend on minicircle size, and thus vary among different species of the
68   Kinetoplastea (Jakob et al., 2016; Jensen & Englund, 2012).

69   Replication of this highly organized DNA network requires the organism to release the individual DNA
70   molecules from catenation to neighboring DNA circles (Jensen & Englund, 2012). The minicircles thus
71   are released from the network prior to replication and move to two opposing poles of the kDNA disc

2

72   (known as the antipodal sites) where they are then replicated and reattached to the network

73   (Amodeo et al., 2022; Jensen & Englund, 2012). Maxicircles on the other hand, are believed to

74   remain attached to the network throughout the replication process. Subsequent segregation of the

75   duplicated kDNA is organized by the basal body (BB) of the flagellum (Ogbadoyi et al., 2003;

76   Schneider & Ochsenreiter, 2018). To allow for coupling of kDNA segregation and BB separation prior

77   to cytokinesis, the kDNA remains physically attached to the proximal end of the BB throughout the

78   cell cycle. This connection, spanning the cytosol, the mitochondrial membranes and the

79   mitochondrial matrix, has been termed the tripartite attachment complex (TAC, (Ogbadoyi et al.,

80   2003)). The TAC not only allows for coordinated segregation of the kDNA, but also anchors the kDNA

81   to its position throughout the cell cycle. As the TAC has to bridge three biochemically distinct regions

82   of the cell to reach from the BB to the mitochondrial DNA, it has been subdivided into three

83   substructures: i) the exclusion zone filaments (EZFs) connecting the BB and the pro-basal body (pBB)

84   to the outer mitochondrial membrane (OMM), ii) the differentiated mitochondrial membranes (DMs,

85   containing a unique set of TAC-specific proteins) and iii) the unilateral filaments (ULFs) that span the

86   distance between the inner mitochondrial membrane (IMM) and the kDNA itself (Ogbadoyi et al.,

87   2003).

88   Over the past decades, several components of the TAC have been identified (Amodeo et al., 2022;

89   Schneider & Ochsenreiter, 2018). While most of them localize to the DMs or the ULFs, it seems that

90   the EZF protein p197 spans the entire exclusion zone (Aeschlimann et al., 2022; Gheiratmand et al.,

91   2013). Its N-terminus localizes at the OMM, while the C-terminus localizes to the proximal end of the

92   BB/ pBB (Aeschlimann et al., 2022). In addition, p197 contains a central section of 26-28 nearly

93   identical repeats of 175-182 amino acids (Aeschlimann et al., 2022; Naguleswaran et al., 2021).

94   Because of its large size, we assume the repeat section to be structurally highly important for the

95   function of p197. p197 stably anchors the BB to the DMs, while tolerating the extensive remodeling

96   processes we observe across the *T. brucei* cell cycle. Interestingly, the amino acid sequence of the

97   ortholog of p197 found in the closely related parasite *Trypanosoma cruzi* (Tcp197) is more than 70 %

98   similar in the terminal domains, but does not contain a repeat section in the middle part of the

99   protein (Aeschlimann et al., 2022). Consequently, the *T. cruzi* protein is much shorter. Experimental

100   replacement of the *T. brucei* p197 repeat section with the corresponding central region of the *T. cruzi*

101   ortholog demonstrates that the *T. cruzi* protein is not able to complement for the function of the

102   repeat section in *T. brucei* p197 (Aeschlimann et al., 2022). This difference in the composition of p197

103   is also reflected by differences in cell cycle dynamics observed between the two parasites. While the

104   cell cycle of *T. brucei* has been shown to include a rotation of the new BB around the old BB prior to

105   kDNA segregation, a similar process seems not to take place in *T. cruzi* (Elias et al., 2007; Vaughan &

106   Gull, 2016). In fact, *T. cruzi* was shown to delay migration and repositioning of the new BB until after

107   the two daughter cells have been generated asymmetrically (Elias et al., 2007).

108   To better understand how p197 functions, we investigated the structural organization of the

109   exclusion zone using cryo-electron tomography (cryo-ET). *T. brucei* cells are too thick to be imaged

110   directly by cryo-ET of whole cells. At the TAC region, the average cell is about two micrometers thick.

111   Typically, transmission electron microscopy (TEM) is only feasible for samples with a maximum

112   thickness of about 500 nm, as thicker samples will yield images of a very low contrast due to inelastic

113   scattering of the electron beam. To circumvent this limitation, we followed two complementary

114   approaches. On the one hand, we thinned the cells before imaging them by cryo-ET; on the other

115   hand, we imaged anucleated cells, which are within the acceptable thickness range. For the first

116   approach we used cryo-focused ion beam (FIB) milling to prepare thin lamellae through vitreously

117   frozen cells (Marko et al., 2007; Schaffer et al., 2017). While very effective in creating thin samples,

118   cryo-FIB milling significantly limits throughput. Therefore, to collect a large dataset, we followed the

119   second approach. As previously demonstrated by Sun and colleagues, anucleated trypanosomes,

120   commonly referred to as zoids, are considerably thinner than their nucleated counterpart and are

121   suitable for cryo-ET (Robinson et al., 1995; Sun et al., 2018).

Results

123   To get an overview of the TAC structure *in situ*, we performed cryo-ET on vitrified wild type procyclic

124   trypanosomes. We thinned down the sample by cryo-FIB milling. The complete workflow from

125   sample preparation, to tilt-series acquisition and data processing is shown in Figure 1 A and detailed

126   in the materials and methods section. A series of three positions across the z-axis of a tomogram

127   generated with this approach is shown in Figure 2 A. The zoom-in images in Figure 2 B show a

128   magnified view of the TAC area.

129   The cytosolic and membraneous parts of the TAC are nicely resolved in cryo-ET of cryo-FIB milled *T.*

130   *brucei* (Figure 2 A). When milled at the corresponding position, the BB, the kDNA pocket of the

131   mitochondrion and the kDNA itself are clearly visible. Furthermore, the EZFs of the TAC are well-

132   resolved and marked in the zoomed images in Figure 2 B (arrowheads).

133   While the area of interest was well-resolved in the data generated with this method, we decided to

134   only acquire a few data sets using this method, while collecting most of our data using zoids, which

135   are thin enough for whole-cell cryo-ET (Sun et al., 2018). Zoids can be generated through the

136   depletion of TbCentrin4, a protein involved in nuclear division and cytokinesis (Shi et al., 2008; Sun et

137   al., 2018).

138   Procyclic *T. brucei* cells were transfected with an RNAi construct targeting the ORF of TbCentrin4.

139   Additionally, we generated a TbCentrin4 p197 double RNAi cell line. p197 RNAi causes the

140   disassembly of the entire TAC including the EZFs (Hoffmann et al., 2018). The combination of

141   TbCentrin4 RNAi with the knockdown of p197 generated TAC-depleted zoids (tdzoids) that we used

142   as a control cell line.

143   The workflow to generate tomographic data on zoid cells is schematically shown in Figure 1 B. To

144   increase the relative number of slim trypanosomes in our sample, we aimed to achieve a high

145   percentage of zoids in the population. As described by Shi and colleagues, TbCentrin4 RNAi only

146   causes a fraction of the population to end up in zoid state (~40 % after 72 h of induction, (Shi et al.,

147   2008)). After expressing the RNAi construct for 65 h, we therefore enriched the TbCentrin4

148   knockdown population for zoids with a series of centrifugation steps (as described by (Sun et al.,

149   2018)). The final population consisted to 80 % of zoids (distribution of nucleus-/kinetoplast-content

150   shown in Figure 1 C). The enriched zoids where then plunge frozen and imaged by cryo-ET.

151 The TbCentrin4 p197 double RNAi cell line was treated as were TbCentrin4 RNAi cells. The
152 enrichment resulted in a concentration of 50 % tdzoids in the final population (karyotype distribution
153 in Figure 1 D). While this ratio is considerably lower than the values reached for zoids, it is worth
154 mentioning that only 8 % of the cells in the enriched population retained the kDNA. Thus, the
155 probability of imaging a tdzoid containing an intact TAC was very low.

156 TbCentrin4 RNAi generates zoids that are suitable for studying the TAC area by cryo-ET
157 TbCentrin4 localizes to the Golgi-associated bilobe structure and to the BBs (Shi et al., 2008). Hence,
158 the protein also localizes close to the TAC. Because of this spatial proximity, we wanted to exclude
159 any effect on the TAC due to TbCentrin4 knockdown (Figure 2 C, D).

160 We performed immunofluorescence microscopy of fixed TbCentrin4 RNAi cells and of TbCentrin4 and
161 p197 double RNAi cells that had either been induced for the RNAi construct(s) for 65 h or not (Figure
162 2 C). To assess the presence of the TAC in TbCentrin4 RNAi zoid cells, we immuno-labelled the TAC
163 component TAC102. We labelled the pBB and BB with the YL1/2 antibody (labelling tyrosinated
164 tubulins at the BB and pBB, (Kilmartin et al., 1982)), while we stained DNA with DAPI. Upon induction
165 of the RNAi construct we observe zoids (recognizable by the absence of nuclear DAPI signal). Such
166 zoids consistently retained their kDNA signal at the posterior end of the cell. Furthermore, we
167 observed that all cells remained TAC102 and YL1/2 positive, with both signals localizing similar to
168 wild type cells.

169 TbCentrin4 p197 double RNAi cells on the other hand, were devoid of nuclear DNA and of kDNA, as
170 expected. Furthermore, TAC102 signal was absent in TbCentrin4 p197 double RNAi zoids, while the
171 YL1/2 signal was retained. The loss of TAC102 in these cells was expected, as TAC102 localization
172 depends on the presence of p197 (Hoffmann et al., 2018). The BB and pBB, and thus YL1/2 signal,
173 was not affected by TAC depletion, as previously reported (Hoffmann et al., 2018). These
174 experiments indicate that the TAC remained intact after TbCentrin4 knockdown, while p197
175 knockdown led to the generation of kinetoplast-free, TAC-depleted zoid cells (tdzoids).

176 To further support an intact TAC morphology in zoid cells, we imaged by TEM chemically fixed and
177 resin-embedded wild type cells and zoids (Figure 2 D). More than 40 TAC regions in either uninduced
178 or induced TbCentrin4 RNAi cells were observed and no difference in TAC morphology was visible.
179 Under both conditions, the area between the mitochondrial kDNA pocket and the (p)BB was devoid
180 of ribosomes, confirming that the TAC was not perturbed by the zoid induction.

181 Morphology of the TAC area in *T. brucei* zoids
182 In many of our zoid cryo-electron tomograms, we could readily identify the TAC and surrounding
183 structures such as the pBB, the BB, the flagellar pocket, the microtubule quartet and the
184 mitochondrial kDNA pocket (Figure 3).

185 The overall organization we observed by cryo-ET matches our expectations from observations
186 previously made by TEM of chemically fixed and resin-embedded wild type trypanosomes and
187 isolated cytoskeletons (Ogbadoyi et al., 2003). Yet, for the first time, we observed the TAC region free
188 of artifacts induced by chemical fixation and resin embedding. All cell membranes, including the

189 mitochondrial double membrane, had a smoother appearance than in chemically fixed and resin-
190 embedded samples (compare Figure 2 D with Figure 3 A, B). The kDNA did not appear as dark as in
191 fixed and stained preparations. This is partly due to the low contrast in the relatively thick area of the
192 trypanosome, and partly due to the absence of heavy-metal staining.

193 Some TAC components could be visualized with an unpreceded level of detail. Between the proximal
194 end of the BB and pBB, in the ribosome-free exclusion zone, we could clearly identify filaments,
195 namely the EZFs (arrowheads in Figure 3 B, 3D-segmentation in Figure 3 C). The filaments are thin
196 and wavy, and span the entire region between the BB and the OMM or the pBB and the OMM,
197 respectively. In some cells we spotted dozens of filaments, while in other tomograms, we could only
198 see a few. We believe the variability in filament count to result from low contrast due to fluctuations
199 in cell thickness, ice quality and precision of tilt-series alignment, rather than from an absence of
200 filaments. The EZFs were clearly visible in 30 % of our tomograms. To confirm that the filaments were
201 indeed part of the TAC, we acquired over 30 tomograms of tdzoids. No filamentous structures
202 between the (p)BB and the OMM could be found in any of them (Figure S 2). Instead, the area
203 contained ribosomes, similar to the rest of the cytoplasm. This demonstrates that in the absence of
204 p197, the exclusion zone and its filaments are not present.

205 Inside the mitochondrion, we did not observe any filamentous structures that would correspond to
206 the ULFs, i.e. intramitochondrial components of the TAC. This is likely because the density of the ULFs
207 is similar to the density of the mitochondrial matrix. We observed structures connecting the outer
208 and inner mitochondrial membranes in the TAC area. These could be the well characterized OMM
209 components of the TAC (pATOM36, TAC40, TAC42, TAC60) connecting to the IMM component p166
210 (Käser et al., 2016, 2017; Schnarwiler et al., 2014; Zhao et al., 2008). However, we observed similar
211 structures in the area outside the TAC. The current resolution did not allow us to assess whether they
212 differed. Nonetheless, the intermembrane distance is significantly smaller in the TAC area (8.2 ± 0.9
213 nm) than outside of it (9.9 ± 1.3 nm) (Figure 4 B). This suggests that the connection of TAC60 in the
214 OMM to p166 in the IMM influences the mitochondrial intermembrane distance (Schimanski et al.,
215 2022). This is in line with a different protein composition within the DMs, which was previously
216 reported (Käser et al., 2017; Ogbadoyi et al., 2003; Schnarwiler et al., 2014).

217 We measured the minimal distance between the proximal face of the BB and the OMM, or the pBB
218 and the OMM, respectively (Figure 4 C). pBBs were located on average 63 ± 81 nm away from the
219 OMM, which is significantly less than the average distance of 145 ± 123 nm between BBs and the
220 OMM. Furthermore, in 70 % of the cells, the pBB was closer to the OMM than the mature BB.

221 The exclusion zone filaments are highly flexible and allow a wide range of movement
222 for the basal body and pro-basal body
223 As mentioned before, the orientation of the BBs towards each other and towards the mitochondrial
224 membranes and kDNA was highly variable (examples depicted in Figure S 1). To quantify the extent
225 of this observed diversity, and to enable us to spot potential preferred orientations, we measured
226 the angles of the respective structures in relation to each other (Figure 5). With mean angles of 31.6
227 ± 31.3° and 35.4 ± 30.1°, the orientation of the BB and pBB in respect to the membranes was not

6

228 significantly different. The mean angle between the BB and pBB was 48.5 ± 39.8°. More striking than

229 the mean angles however, was the wide spread of the data points. In Figure 5 B one can appreciate

230 that the angle ranged from -78° to 84° for the BB, and from -52° to 87° for the pBB. Furthermore, the

231 angle between BB and the pBB was equally as variable, with a range of 1° to 162° (Figure 5 D).

232 Despite the wide spread, the most extreme values were quite rare overall. This is reflected by the

233 standard deviations indicated in Figure 5 B and D. The histograms shown in Figure 5 C and E

234 demonstrate that the vast majority of the observed angles between BB / pBB and the mitochondrial

235 membranes were positive, comprised between 0° and 90°, and peaking in abundance around 45°.

236 Small angles close to 0° were most abundant between the two BB types.

237 ## Structural analysis of individual exclusion zone filaments

238 Based on the available literature on the TAC and its components, we assumed p197 to be the protein

239 we observe as the EZF in cryo-ET. In a recent study, p197 has been shown to span the entire

240 exclusion zone (Aeschlimann et al., 2022). Using ultrastructure expansion microscopy, Aeschlimann

241 and colleagues demonstrated that the N-terminus of p197 localizes to the DMs, while the C-terminus

242 of the protein is localized to the BB and pBB. Between the N-terminal and C-terminal domains, p197

243 contains at least 26 nearly identical repeats of 175 - 182 amino acids each(Aeschlimann et al., 2022;

244 Naguleswaran et al., 2021). p197 being the EZF is well in line with the observed absence of EZFs in

245 cells depleted of p197 (tdzoids, Figure S 2).

246 The structure of p197 is not known. Given the flexibility of the EZFs, we did not attempt to perform

247 subtomogram averaging of them. Instead, we followed an integrative approach, combining structural

248 prediction and structural information that we could extract from our tomograms.

249 We measured the diameter of 100 EZFs from ten high contrast tomograms to be on average 4.57 ±

250 0.89 nm (Figure 6 B). We then measured the length of the EZFs in 22 tomograms. In each of these

251 tomograms, we manually segmented five filaments and measured their length (Figure 6 C). The

252 average length was 417.5 ± 89.2 nm, with considerable variation, ranging from 230 nm to 625 nm.

253 As the central repeat section of p197 makes up most of the protein, it likely corresponds to the

254 filamentous structure of the EZFs observed in cryo-ET. We therefore modelled the repeat section

255 with AlphaFold2 (Figure 6 D, (Jumper et al., 2021)). Due to hardware limitations, we could not model

256 the full protein. Instead, we modelled a shorter sequence composed of the N-terminal domain, six

257 repeats and the C-terminal domain (construct overview in Figure S 4). While the N- and C-terminal

258 prediction was unstructured and had a low confidence score, a repetitive pattern of coiled coils is

259 predicted for the central repeat section (Figure 6 D, Figure S 3). Each repetitive unit is composed of

260 three antiparallel α-helices of 49, 51 and 49 amino acids, respectively, and an α-helical linker of 20

261 amino acids. This fold resembles the fold of the spectrin repeat (Liem, 2016). We therefore further

262 refer to the p197 repetitive unit as spectrin-like unit.

263 To verify plausibility of the AlphaFold2 prediction, we compared the dimensions of the predicted

264 p197 filaments to those of the filaments in our cryo-ET data. From a low-resolution map of the

265 spectrin-like unit (calculated to a resolution of 1.5 nm) we measured the diameter at six positions

266 along a spectrin-like unit and one position within the linker helix (Figure 6 E, top). Based on these

267   measurements we expect diameters ranging from 2.2 to 4.2 nm in the spectrin-like unit, while we

268   expect values as small as 2 nm in the linker region. We then further calculated the theoretical length

269   of the entire repeat section of p197 (assuming 26 repeats, as annotated in EATRO1125

270   (Naguleswaran et al., 2021)) to a value of 286 nm (Figure 6 E, bottom). The predicted length did not

271   match most of our measurements in tomograms (Figure 6 C, E). While a few measurements are in

272   the range of the predicted length, most of the filaments are considerably longer. Considering the

273   variability of the (p)BB distance to the OMM (Figure 4 C), this matches our expectations. We

274   therefore assume the structure predicted by AlphaFold2 to represent only one of several possible

275   conformations of p197.

276   Also, the predicted diameter of individual p197 molecules did not entirely match the filament

277   diameters measured in cryo-ET (Figure 4 B, B). While some measurements fall within the range of

278   the predicted diameter of the spectrin-like unit, others suggest a diameter up to 1.5-fold the

279   expected values. Such a discrepancy might result from delocalization effects of the contrast transfer

280   function and the missing wedge effect. It could, on the other hand, reflect potential oligomerization

281   of p197, or decoration of the protein with small proteins of unknown identity.

282   We conclude that p197 adopts the shape of a flexible filament consisting of an array of spectrin-like

283   units. These repetitive units are flanked by the terminal domains that provide anchorage to the BB

284   and downstream TAC components.

Discussion

285

286   The TAC is likely unique to the Kinetoplastea, and yet, some of its features show similarities to other

287   systems and processes. Conceptually and functionally, the TAC closely resembles the mitotic

288   kinetochore structure. This analogy has been put forward in a recent publication, based on the

289   shared role in DNA segregation and the involvement of centrioles in the process (Amodeo et al.,

290   2020). Centrioles are a common feature in many eukaryotic species, acting as microtubule organizing

291   centers (MTOCs) and forming the base of flagella or cilia. The TAC in *T. brucei* serves as a striking

292   example of divergent evolution, where a widespread structure has been repurposed for a unique

293   function. At the same time, it is an example of convergent evolution, where two independent sets of

294   proteins have evolved to perform the same function of separating replicated DNA.

295   To get a better understanding of how trypanosomes and other kinetoplastid species utilize their BBs

296   to orchestrate segregation of a complex DNA network, it is crucial to observe the TAC structure in its

297   native unperturbed environment. In this study we structurally characterized the EZFs and the DMs of

298   the TAC, by applying cryo-ET to a genetically engineered cell line.

299   While thin sections produced by ultramicrotomy rarely simultaneously capture the BB, pBB and a

300   middle section of the kDNA in a single cell, whole-cell tomography enabled us to observe these

301   structures together. Tomographic imaging in intact zoid allowed us to avoid the detection bias

302   created by manual search of the area of interest in fixed section TEM. When we image thin sections

303   of chemically-fixed, resin-embedded cells, a cross-sectioned stained kDNA is very easy to spot, even

304   at relatively low magnifications. We then zoom into those regions specifically, and search for a BB. If

305   we see both structures, we are confident that, if there were a TAC, we would see it. In whole-cell

306 imaging we don't rely on this selective acquisition process. Instead, we can image the TAC region in

307 any cell within the sample. Cryo-ET therefore allows for a more comprehensive analysis of samples,

308 as opposed to the limited perspective provided by targeted search in 2D imaging. Our data shows

309 that there is a high degree of orientational diversity within the TAC area, which is not typically

310 captured by 2D imaging.

311 Qualitative observation of the TAC area in intact trypanosomes revealed the overall architecture of

312 the complex (Figure 2 an Figure 3). We could clearly identify the EZFs. Quantitative analysis of the

313 distance between the (p)BB and the DMs showed that the pBB often resides closer to the OMM, than

314 the mature BB does (Figure 4 B). Furthermore, we could distinguish the DMs from the surrounding

315 area of the mitochondrial membranes. Our analysis of the mitochondrial membranes demonstrated

316 that the inter-membrane distance in the DM area was 17 % smaller compared to the surrounding

317 area (Figure 4 C).

318 To investigate the structure of the EZF protein p197, we used an integrative approach combining

319 quantitative analysis of cryo-electron tomograms, sequence analysis, AI-based structural predictions

320 and information gathered from the literature (Figure 6). The experimental results obtained from the

321 analysis of cryo-ET data provide insights into the diameter and length of the individual filaments

322 (Figure 6 B, C). Structural predictions of the repeat section of p197 using AlphaFold2, suggest an

323 organization in spectrin-like α-helical bundles (spectrin-like units, Figure 6 D). The spectrin-like units

324 are predicted to be connected via an α-helical linker of sufficient length to enable the alignment of

325 spectrin-like units to a filamentous stretch of coiled coils.

326 To align the AlphaFold2 prediction with the cryo-ET data, we extrapolated the six-repeat p197

327 predicted by AlphaFold2, to the full length of 26 repeats, and calculated the length of the repeat

328 section to 286 nm. This number aligns well with the shortest filament lengths measured in cryo-ET

329 (l_{min} = 230 nm, C). However, this theoretical length does not fit the length of most of the observed

330 filaments (417.5 ± 89.2 nm, Figure 6 C). We therefore suggest that the structure predicted by

331 AlphaFold2 only reflects the most stable state of the protein, while many filaments that we observed

332 in cryo-ET likely assume different conformations in response to tensions arising from BB movement.

333 One source of BB movement is imposed by the propelling movement of the flagellum (Figure 7 A).

334 We assume it to cause a slight but constant tumbling of the BB.

335 Other sources of BB movements include the cell cycle dependent repositioning of the basal bodies in

336 preparation of cell division. The first of these movements is the rotation of the new BB/pBB pair

337 around the old BB during kinetoplast S-phase (Figure 7 B). This process displaces the new BB/pBB

338 pair to a position posterior of the parental BB (Vaughan & Gull, 2016). Vaughan and colleagues

339 showed that this rotation happens at late stages of pBB outgrowth, when the transition zone is fully

340 formed and the new pBBs have been nucleated next to the old flagellum and the freshly matured BB

341 (Vaughan & Gull, 2016). Our data show that the assembly of p197 at the new BB happens before

342 these events. The filaments are fully assembled at the maturing BB before the nucleation of a fresh

343 set of pBBs (Figure 3). This indicates that filaments are present at the time of BB rotation.

9

344   The second cell cycle dependent BB movement happens after the outgrowth of the new axoneme

345   (Figure 7 C). At this stage, the kDNA has been fully replicated, and the two BB/pBB pairs separate

346   (Schneider & Ochsenreiter, 2018). The connection between the BBs and the kDNA (provided by the

347   TAC) allows for segregation of the kDNA along with BB separation (Ogbadoyi et al., 2003; Schneider &

348   Ochsenreiter, 2018).

349   Collectively, cell motility, BB rotation and BB separation all require p197 to be sufficiently elastic to

350   resist variable levels of mechanical force throughout the cell cycle. Our measurements of the

351   distance and angular position of the BBs relative to the outer mitochondrial membrane clearly

352   demonstrate that p197 indeed provides the flexibility suggested by its function (Figure 4 and Figure

353   5). The distance of the BB to the OMMs was highly variable, which supports our claim of a need for

354   flexibility of the TAC (Figure 4). The observation of the angular variability between the (p)BB and the

355   OMM further demonstrates the extend of flexibility p197 provides (Figure 5).

356   We hypothesize that under tension, individual spectrin-like units of p197 unfold to a single α-helix

357   (Figure 7 D). The number of unfolded spectrin-like units should depend on the force applied to the

358   individual filament. When all 26 units are unfolded, p197 reaches a maximum length of 690 nm. The

359   predicted range of 286 nm to 690 nm aligns well with our observations in cryo-ET (230 – 625 nm,

360   Figure 6 C). Previous research has demonstrated that temporary unfolding, or elasticity, plays a key

361   role in the function of many spectrin-repeat containing proteins, such as the giant muscle protein

362   titin (Djinovic-Carugo et al., 2002; Tskhovrebova et al., 1997). An engineered polymeric protein

363   consisting of four identical spectrin domains was also shown to have elastic properties consistent

364   with the unfolding pattern we predict for p197 (Lenne et al., 2000).

365   In case of p197, the mechanical force can vary not only over time, but also between the different

366   filaments of a single BB at any given moment (Figure 7 E). We assume that both the releasable coiled

367   coil of the spectrin-like unit and the α-helical linker contribute to the considerable variation in (p)BB

368   positioning we observe in cryo-ET (Figure 4, Figure 5).

369   It was shown that deletion of the p197 spectrin-like units in *T. brucei* leads to loss of mitochondrial

370   DNA, despite the proper localization of the protein and its ability to bind the BB and the OMM

371   (Aeschlimann et al., 2022). The absence of spectrin-like units in the *T. cruzi* ortholog is consistent

372   with the differences in cell cycle dynamics observed between the two parasites. (Elias et al., 2007;

373   Vaughan & Gull, 2016). The absence of spectrin-like units in the *T. cruzi* ortholog of p197 further

374   implies that a non-extendable, α-helical domain such as the one found in *T. cruzi* is sufficient to

375   tolerate the effects of cell motility and BB separation – at least in *T. cruzi*. We therefore suggest that

376   the most important role of the spectrin-like unit is the protein's structural response to the cell cycle

377   dependent BB rotation in *T. brucei*.

378   To confirm the plausibility of the AlphaFold2 model, and to assess the oligomeric state of p197, we

379   compared the diameter of the predicted spectrin-like unit with the diameter of the filaments as

380   measured in cryo-ET. The range of 2 – 4.2 nm measured in the predicted structure is similar, but

381   smaller than the range measured in the cryo-ET data (2.4 – 6.6 nm, B, Figure 6 A). While this

382   discrepancy may reflect an artefact of the contrast transfer function and the missing wedge of the

383   tomographic data, it may also indicate p197 to oligomerize. Oligomerization of spectrin-repeat

384   containing proteins is not unusual and has been shown for other spectrin-repeat proteins, such as

385   spectrin or α-actinin (Djinovic-Carugo et al., 2002; Speichers et al., 1992). Alternatively, the protein

386   may be decorated by other proteins that stabilize the filaments or assist correct folding and release

387   of spectrin-like units.

388   In summary, our study describes the structure of the exclusion zone of the TAC. Using an integrative

389   approach, we propose a model of the molecular structure of p197. It contradicts the notion of the

390   TAC having a rather rigid structure suggested by earlier studies. More importantly however, the

391   finding that p197 acts as a molecular spring provides an example of how a giant protein provides

392   flexibility and stability for a dynamic cellular system.

Material and Methods

Trypanosoma brucei cell culture conditions

395   Procyclic form 29-13 asynchronous *T. brucei* cells were cultured in semi-defined medium-79 (SDM-

396   79) supplemented with 10 % FCS, 15 µg/ml geneticin and 25 µg/ml hygromycin at 27° C (Wirtz et al.,

397   1999). The cell line is part of the established collection of the Institute of Cell Biology, University of

398   Bern, Bern, Switzerland.

399   From the 29-13 cell line, the two RNAi cell lines TbCentrin4 RNAi and TbCentrin4 p197 double RNAi

400   were generated. Depending on the cell line, 5 µg/ml phleomycin and/or 10 µg/ml blasticidin was

401   added to the media (see below). For RNAi induction, 1 µg/ml tetracycline was used.

Cloning of RNAi constructs

403   To clone the TbCentrin4 RNAi construct, we inserted base pairs 19-438 of the ORF (TREU927) into the

404   pFC-4 vector. The sequence was obtained by PCR: FWD-primer: 5' –

405   GTAAAAGCTTGGATCCGAACAGATCCGTGAAGCG – 3'; REV-primer: 5'

406   GTAATCTAGACTCGAGCATCTGCATCATGACGCTC – 3'; template DNA: NYsm DNA isolate. Using the

407   restriction sites (HindIII, BamHI, XbaI and XhoI) introduced by the primers, the target sequence was

408   inserted twice (in opposite direction) to encode for a hairpin dsRNA. The pFC-4 plasmid contains

409   blasticidin resistance. The p197 RNAi construct was previously described (Hoffmann et al., 2018). It

410   encodes a hairpin dsRNA targeting the p197 ORF, and the phleomycin resistance gene.

Trypanosoma brucei transfections

412   To obtain the TbCentrin4 RNAi and TbCentrin4 p197 double RNAi cell lines, we transfected cells with

413   the constructs described above. We integrated the constructs by homologous recombination. 10^8 29-

414   13 PCF cells, or TbCentrin4 RNAi cells were used. The transfection mixtures consisted of 10 µg of

415   linearized plasmid in 110 µl transfection buffer (90 mM sodium phosphate (pH 7.3), 5 mM KCl, 0.15

416   mM CaCl$_2$, 50 mM HEPES (pH 7.3))(Burkard et al., 2007). Cells were pelleted at 2'500 rcf for 8 min,

417   mixed carefully with the transfection mixture and electroporated with the Amaxa Nucleofector

418   (program X-014)(Schumann Burkard et al., 2011). After transfection, the cells were recovered in

419   antibiotic free SDM-79 for 20 h. After the recovery, we added the respective antibiotics to select for

420 integration of the transfected constructs. To select for TbCentrin4 RNAi, we used 10 µg/ml

421 blasticidin. For p197 RNAi, 5 µg/ml phleomycin were used.

Immunofluorescence analysis

423 10^6 cells were pelleted for 3 min at 1800 rcf. Cells were washed with 1 ml PBS, resuspended in 20 µl

424 PBS and spread on a glass slide. After settling, cells were fixed for 4 min with 4 % paraformaldehyde

425 in PBS. Following fixation, they were permeabilized for 5 min with 0.2 % Triton-X 100. The sample

426 was then blocked with 4 % bovine serum albumin in PBS for 30 min. Cells were incubated with

427 primary and secondary antibodies (diluted in blocking solution) for 45-60 min as follows: rat YL1/2

428 antibody detecting tyrosinated tubulin, which is found in the BB (Kilmartin et al., 1982)(a kind gift of

429 Keith Gull) 1:10'000, monoclonal mouse anti-TAC102 antibody (Trikin et al., 2016) 1:5'000, Alexa

430 Fluor® 488 goat anti-rat IgG (H+L)(Nanoprobes/FluoroNanogold) 1:1000, Alexa Fluor® 647 goat anti-

431 mouse IgG (H+L)(Life technologies) 1:1000. After each antibody incubation step, cells were washed 3

432 x with 0.1 % Tween-20 (in PBS). A final wash with PBS was performed before mounting the cells in

433 ProLong® Gold Antifade Mounting medium with DAPI (4',6-diamidine-2-phenylindole)(Invitrogen).

Fixed section transmission electron microscopy

435 Trypanosomes were grown as described above, harvested and centrifuged at 2500 rcf for 5 min. The

436 pellets were fixed with 2.5 % glutaraldehyde in 0.15 M HEPES pH 7.41 at 4° C for at least 24 h. They

437 were then washed with 0.15 M HEPES three times for 5 min, post-fixed with 1 % OsO4 in 0.1 M

438 sodium cacodylate buffer at 4° C for 1 h, washed with 0.05 M maleate-NaOH buffer three times for 5

439 min. Subsequently the cells were dehydrated in 70, 80, and 96 % ethanol for 15 min each, at room

440 temperature. Then the cells were immersed in 100 % ethanol three times for 10 min, in acetone two

441 times for 10 min, and finally in acetone-epon (1:1) overnight, at room temperature. Cells were then

442 embedded in pure epon and left to harden at 60° C for 5 days. Ultrathin sections (70−80 nm) were

443 produced with an ultramicrotome UC6 (Leica Microsystems). The sections, mounted on 200 mesh

444 copper grids, were stained with uranyless and lead citrate with an ultrostainer (Leica Microsystems).

445 Sections were then examined with a transmission electron microscope (Tecnai Spirit, 80 kV)

446 equipped with Olympus-SIS Veleta CCD camera.

Sample preparation for cryo-electron tomography of zoids

448 TbCentrin4 RNAi or TbCentrin4 p197 double RNAi PCF cells were RNAi induced for 65 h. The cells

449 were then harvested by centrifugation at 2500 rcf, for 8 min. They were then resuspended in serum-

450 free SDM-79 to a concentration of $2 \cdot 10^7$ cells/ml, and treated with a series of centrifugation steps:

451 26 rcf for 2 min, 68 rcf for 3 min, 210 rcf for 5 min. Then, the upper 35 % of the sample were

452 collected for further centrifugation: 210 rcf for 3 min, 340 rcf for 5 min. We then collected the upper

453 55 % of this fraction, before centrifuging again, at 345 rcf for 3 min. At this point we collected the

454 upper 60 % of the sample, and pelleted all cells remaining in this faction, by centrifugation at 1800 rcf

455 for 7 min. The cells were washed in PBS, and then resuspended to a final concentration of $4 \cdot 10^7$

456 cells/ml. 10 nm gold beads (Aurion, OD520 = 2.0) were added 1:10 v:v. 3 µl of this sample were

457 placed on a glow-discharged EM grid (lacey carbon films on Cu 200 mesh, Quantifoil Micro Tools),

458 blotted from the back side for 3 s, and plunged into liquid ethane at a temperature of ≤ -170° C. The

459 grids were stored in liquid nitrogen, until further use.

460   Tilt-series were acquired on Titan Krios transmission electron microscopes (Thermo Fisher Scientific)

461   operating at 300 kV. The microscopes used were equipped with post-column energy filter, K2

462   (Gatan), K3 (Gatan) or Falcon4 (Thermo Fisher Scientific) direct electron detector, and in some cases,

463   volta phase plate was used to enhance contrast at low defocus. Using SerialEM, tomograms were

464   acquired as dose-symmetric tilt-series in 2° increments, ranging from -60° to +60°. A total electron

465   dose of $120e^-/Å^2$ was applied.

Sample preparation with focused ion beam milling

467   Cells were blotted on EM grids (R 2/1 holey carbon 200 films on Cu 200 mesh, Quantifoil Micro

468   Tools). The grids were first glow-discharged and 4 µl of trypanosome wild-type culture $(2-4 \cdot 10^7$

469   cells/ml) were placed on the grid. Using a Vitrobot Mark 4 (Thermo Fisher Scientific), cells were

470   plunge frozen in a liquid ethane-propane mixture after blotting for 12 s at blotting force -4.

471   Afterwards, grids were clipped into autogrid support rings with a cut-out that allows access to the ion

472   beam at low angle (Thermo Fisher Scientific) and stored in liquid nitrogen until being used for FIB

473   milling.

474   Cryo-FIB milling was performed as described previously (Schaffer et al., 2017) with an Aquilos 2 dual-

475   beam FIB/ SEM instrument (Thermo Fisher Scientific). In the FIB/SEM chamber, grids were coated

476   with a layer of organometallic platinum using a gas injection system to protect the sample surface.

477   Micro-expansion joints (relief cuts) were milled to prevent lamella from bending (Wolff et al., 2019).

478   A gallium ion beam was used for the milling. Owing to the small size of individual trypanosome cells,

479   small clusters of cells were milled at a low angle (14-15°) to form short lamellae of 70-200 nm

480   thickness. After milling, grids were transferred into a Titan Krios transmission electron microscope

481   (Thermo Fisher Scientific), operating at 300 kV with a post-column energy filter (GIF Quantum LS,

482   Gatan), and a direct detector camera (K2, Gatan). A total electron dose of $60-80e^-/Å^2$ was distributed

483   over a tilt range of -60° to +60°, with an increment of 2°. SerialEM was used for data collection.

Processing of cryo-electron tomograms

485   After acquisition, tilt-series of cryo-FIB milled trypanosomes were preprocessed using the

486   TOMOMAN pipeline (v.0.6.9)(Wan, 2020) and custom MATLAB scripts. Raw frames of all tilt-series

487   (including cryo-FIB milled trypanosomes as well as TbCentrin4 zoids and tdzoids) were then aligned

488   using MotionCor2 (v1.3.2 or v.1.4.7)(Zheng et al., 2017). Then, each cryo-electron tomogram was

489   reconstructed in IMOD (v4.12.0)(Mastronarde & Held, 2017), analysed visually, and tomograms were

490   selected for further processing. This processing included deep learning based denoising using cryo-

491   CARE (v0.1.1)(Buchholz et al., 2019) and in a few cases, manual segmentation of structures of

492   interest, using IMOD. Tomograms from cryo-FIB milled trypanosomes were further processed with

493   IsoNet (Liu et al., 2022), to compensate for missing wedge artifacts.

494   Distance measurements were conducted with the "measure" function of the IMOD drawing tools.

495   Filament length was measured by placing contours on the relevant structures, and readout of all

496   contour lengths of the respective IMOD model. Filament diameter was measured from manually

497   selected stretches of well-resolved filaments. The local filament diameter was then measured from

498   the intensity curve along a line drawn orthogonally to the filament direction. The effective diameter

499   was defined as the width of the intensity drop at half its depth. Intermembrane distance was
500   measured using the FIJI macro "InteredgeDistance_v1.0.1_ImageJMacro.txt" found online
501   (https://forum.image.sc/t/imagej-macro-to-measure-distance-between-two-lines-edges/42019). This
502   macro takes two manually segmented lines as an input to return the distance between the two lines
503   at 15 positions along them. The measured values correspond to the distance between centers of the
504   respective membrane.

505   Angle measurements were performed using a custom-made python script. Upon entry of the
506   coordinates of four points and a plane (defined by three points) in 3D space, the script calculates the
507   normal vector of the plane, and the directional vectors of points one and two, and of points three
508   and four, respectively. Based on the normal vector of the plane, and the directional vectors, it then
509   further calculates the angle between each directional vector and the plane, as well as the angle
510   between the two directional vectors. To apply this to our dataset, we defined the mitochondrial
511   membranes in the TAC area as the plane, and the BB and pBB as directional vectors. We manually
512   collected the respective points needed to define 3D orientation of the three objects of interest in the
513   reconstructed tomograms.

514   BB / pBB distance to the mitochondrial membranes, angle measurements and filament length were
515   measured on denoised tomograms acquired without volta phase plate, at defocus values ranging
516   from -2 to -10 µm. EZF diameter was measured on non-filtered, unbinned (pixel size: 0.434 nm)
517   tomograms acquired with volta phase plate, at defocus values of no more than -2.5 µm.

518   ## Circular statistics
519   Since angles are distributed on a circular scale, both angular extremes (close to 0° and close to 360°)
520   are similar in direction, despite their numerical distance. Consequentially, statistical values must be
521   calculated under consideration of this discrepancy from the linear scale (Berens, 2009; Schneiter et
522   al., 2021). The circular mean and corresponding standard deviations where therefore calculated from
523   the following equations:

524     $$\langle \vec{R} \rangle = \frac{1}{N} \sum_{q=1}^{N} \vec{R_q} = (\langle cos\gamma \rangle, \langle sin\gamma \rangle) \qquad (1)$$

525     $$\langle \gamma \rangle_c = arctan_2(\langle sin\gamma \rangle, \langle cos\gamma \rangle) \qquad (2)$$

526     $$S_c = \sqrt{-2ln(R)} \qquad (3)$$

527     $\langle \vec{R} \rangle$ hereby represents the mean resultant vector, which depends on the number N of angles, their
528   respective values $\gamma_1 - \gamma_N$. Each angle γ_q was first transformed into its corresponding unit vector
529     $\vec{R_q} = (cos\gamma_q, sin\gamma_q)$. The direction of $\langle \gamma \rangle_c$ of the mean resultant vector $\langle \vec{R} \rangle$ finally represents the
530   mean direction.

531   The circular analogue to the standard deviation was derived from the length of the mean resultant
532   vector $R = \|\langle \vec{R} \rangle\|$. It lies within the interval [0,1] and is described as S_c.

14

533 Calculations were performed using a python package for circular statistics available on GitHub:

534 https://gist.github.com/kn1cht/89dc4f877a90ab3de4ddef84ad91124e

535 Modelling with AlphaFold2

536 For AlphaFold2 modelling, we used a truncated version of the amino acid sequence of 197

537 (EATRO1125, (Naguleswaran et al., 2021)) consisting of the N-terminal domain, six sequence repeats,

538 one incomplete repeat (as this is also present in the annotated protein sequence), and the C-terminal

539 domain (Figure S 4). Using the open-source code available on github.com AlphaFold2 was run on an

540 in-house workstation. Monomeric p197 was run in AlphaFold2 multimer preset, predicting a total of

541 five models. Model 4 was selected for further processing, based on highest LDDT scores in the repeat

542 section (Figure S 3).

543 The theoretical filament diameter was determined based on a low-resolution map (1.5 nm)

544 generated from the most N-terminal two units of the AlphaFold2 model (mapping performed in

545 Chimera 1.16). Diameters of the filament cross-section were measured at six different positions

546 along the coiled coil and one position within the linker (at each position, the largest and smallest

547 diameter was measured).

548 Acknowledgments

558

References

Aeschlimann, S., Kalichava, A., Schimanski, B., Berger, B. M., Jetishi, C., Stettler, P., Ochsenreiter, T., & Schneider, A. (2022). Single p197 molecules of the mitochondrial genome segregation system of Trypanosoma brucei determine the distance between basal body and outer membrane. *Proceedings of the National Academy of Sciences*, *119*(40). https://doi.org/10.1073/pnas.2204294119

Amodeo, S., Bregy, I., & Ochsenreiter, T. (2022). Mitochondrial genome maintenance - the kinetoplast story. *FEMS Microbiology Reviews*. https://doi.org/10.1093/FEMSRE/FUAC047

Amodeo, S., Hoffmann, A., Fradera-Sola, A., Bregy, I., Baudouin, H., Haenni, B., Zuber, B., Butter, F., & Ochsenreiter, T. (2020). Characterization of two novel proteins involved in mitochondrial DNA anchoring. *BioRxiv*, 2020.07.22.215871. https://doi.org/10.1101/2020.07.22.215871

Berens, P. (2009). CircStat: A MATLAB Toolbox for Circular Statistics. *Journal of Statistical Software*, *31*(10), 1–21. https://doi.org/10.18637/JSS.V031.I10

Braymer, J. J., & Lill, R. (2017). Iron–sulfur cluster biogenesis and trafficking in mitochondria. In *Journal of Biological Chemistry* (Vol. 292, Issue 31, pp. 12754–12763). American Society for Biochemistry and Molecular Biology Inc. https://doi.org/10.1074/jbc.R117.787101

Buchholz, T.-O., Jordan, M., Pigino, G., & Jug, F. (2019). Cryo-CARE: Content-Aware Image Restoration for Cryo-Transmission Electron Microscopy Data. *2019 IEEE 16th International Symposium on Biomedical Imaging (ISBI 2019)*, 502–506. https://doi.org/10.1109/ISBI.2019.8759519

Burkard, G., Fragoso, C. M., & Roditi, I. (2007). Highly efficient stable transformation of bloodstream forms of Trypanosoma brucei. *Molecular and Biochemical Parasitology*, *153*(2), 220–223. https://doi.org/10.1016/j.molbiopara.2007.02.008

Chen, J., Rauch, C. A., White, J. H., Englund, P. T., & Cozzarelli, N. R. (1995). The topology of the kinetoplast DNA network. *Cell*, *80*(1), 61–69. https://doi.org/10.1016/0092-8674(95)90451-4

Djinovic-Carugo, K., Gautel, M., Ylänne, J., & Young, P. (2002). The spectrin repeat: A structural platform for cytoskeletal protein assemblies. *FEBS Letters*, *513*(1), 119–123. https://doi.org/10.1016/S0014-5793(01)03304-X

Elias, M. C., da Cunha, J. P. C., de Faria, F. P., Mortara, R. A., Freymüller, E., & Schenkman, S. (2007). Morphological Events during the Trypanosoma cruzi Cell Cycle. *Protist*, *158*(2), 147–157. https://doi.org/10.1016/J.PROTIS.2006.10.002

Friedman, J. R., & Nunnari, J. (2014). Mitochondrial form and function. *Nature*, *505*(7483), 335–343. https://doi.org/10.1038/nature12985

Gheiratmand, L., Brasseur, A., Zhou, Q., & He, C. Y. (2013). Biochemical characterization of the bi-lobe reveals a continuous structural network linking the bi-lobe to other single-copied organelles in Trypanosoma brucei. *The Journal of Biological Chemistry*, *288*(5), 3489–3499. https://doi.org/10.1074/jbc.M112.417428

595   Hajduk, S., & Ochsenreiter, T. (2010). RNA editing in kinetoplastids. *RNA Biology*, *7*(2), 229–236.
596   https://doi.org/10.4161/rna.7.2.11393

597   Hoffmann, A., Käser, S., Jakob, M., Amodeo, S., Peitsch, C., Týč, J., Vaughan, S., Zuber, B., Schneider,
598   A., & Ochsenreiter, T. (2018). Molecular model of the mitochondrial genome segregation
599   machinery in Trypanosoma brucei. *Proceedings of the National Academy of Sciences of the*
600   *United States of America*, *115*(8), E1809–E1818. https://doi.org/10.1073/pnas.1716582115

601   Hong, M., & Simpson, L. (2003). Genomic organization of Trypanosoma brucei kinetoplast DNA
602   minicircles. *Protist*, *154*(2), 265–279. https://doi.org/10.1078/143446103322166554

603   Jakob, M., Hoffmann, A., Amodeo, S., Peitsch, C., Zuber, B., & Ochsenreiter, T. (2016). Mitochondrial
604   growth during the cell cycle of Trypanosoma brucei bloodstream forms. *Scientific Reports*, *6*.
605   https://doi.org/10.1038/srep36565

606   Jensen, R. E., & Englund, P. T. (2012). Network news: the replication of kinetoplast DNA. *Annual*
607   *Review of Microbiology*, *66*, 473–491. https://doi.org/10.1146/annurev-micro-092611-150057

608   Jumper, J., Evans, R., Pritzel, A., Green, T., Figurnov, M., Ronneberger, O., Tunyasuvunakool, K.,
609   Bates, R., Žídek, A., Potapenko, A., Bridgland, A., Meyer, C., Kohl, S. A. A., Ballard, A. J., Cowie,
610   A., Romera-Paredes, B., Nikolov, S., Jain, R., Adler, J., … Hassabis, D. (2021). Highly accurate
611   protein structure prediction with AlphaFold. *Nature*, *596*(7873), 583–589.
612   https://doi.org/10.1038/s41586-021-03819-2

613   Käser, S., Oeljeklaus, S., Týč, J., Vaughan, S., Warscheid, B., & Schneider, A. (2016). Outer membrane
614   protein functions as integrator of protein import and DNA inheritance in mitochondria.
615   *Proceedings of the National Academy of Sciences*, *113*(31), E4467–E4475.
616   https://doi.org/10.1073/pnas.1605497113

617   Käser, S., Willemin, M., Schnarwiler, F., Schimanski, B., Poveda-Huertes, D., Oeljeklaus, S., Haenni, B.,
618   Zuber, B., Warscheid, B., Meisinger, C., & Schneider, A. (2017). Biogenesis of the mitochondrial
619   DNA inheritance machinery in the mitochondrial outer membrane of Trypanosoma brucei. *PLoS*
620   *Pathogens*, *13*(12), e1006808. https://doi.org/10.1371/journal.ppat.1006808

621   Kilmartin, J. v, Wright, B., & Milstein, C. (1982). Rat monoclonal antitubulin antibodies derived by
622   using a new nonsecreting rat cell line. *The Journal of Cell Biology*, *93*(3), 576–582.
623   https://doi.org/10.1083/jcb.93.3.576

624   Lenne, P. F., Raae, A. J., Altmann, S. M., Saraste, M., & Hörber, J. K. H. (2000). States and transitions
625   during forced unfolding of a single spectrin repeat. *FEBS Letters*, *476*(3), 124–128.
626   https://doi.org/10.1016/S0014-5793(00)01704-X

627   Liem, R. K. H. (2016). Cytoskeletal Integrators: The Spectrin Superfamily. *Cold Spring Harbor*
628   *Perspectives in Biology*, *8*(10). https://doi.org/10.1101/CSHPERSPECT.A018259

629   Liu, Y. T., Zhang, H., Wang, H., Tao, C. L., Bi, G. Q., & Zhou, Z. H. (2022). Isotropic reconstruction for
630   electron tomography with deep learning. *Nature Communications*, *13*(1).
631   https://doi.org/10.1038/S41467-022-33957-8

632   Marko, M., Hsieh, C., Schalek, R., Frank, J., & Mannella, C. (2007). Focused-ion-beam thinning of
633   frozen-hydrated biological specimens for cryo-electron microscopy. *Nature Methods 2007 4:3*,
634   *4*(3), 215–217. https://doi.org/10.1038/nmeth1014

635   Mastronarde, D. N., & Held, S. R. (2017). Automated Tilt Series Alignment and Tomographic
636   Reconstruction in IMOD. *Journal of Structural Biology*, *197*(2), 102.
637   https://doi.org/10.1016/J.JSB.2016.07.011

638   Naguleswaran, A., Fernandes, P., Bevkal, S., Rehmann, R., Nicholson, P., & Roditi, I. (2021).
639   Developmental changes and metabolic reprogramming during establishment of infection and
640   progression of Trypanosoma brucei brucei through its insect host. *PLoS Neglected Tropical*
641   *Diseases*, *15*(9). https://doi.org/10.1371/JOURNAL.PNTD.0009504

642   Ochsenreiter, T., Cipriano, M., & Hajduk, S. L. (2007). KISS: The kinetoplastid RNA editing sequence
643   search tool. *RNA*, *13*(1), 1–4. https://doi.org/10.1261/rna.232907

644   Ogbadoyi, E. O., Robinson, D. R., & Gull, K. (2003). A high-order trans-membrane structural linkage is
645   responsible for mitochondrial genome positioning and segregation by flagellar basal bodies in
646   trypanosomes. *Molecular Biology of the Cell*, *14*(5), 1769–1779.
647   https://doi.org/10.1091/mbc.e02-08-0525

648   Povelones, M. L. (2014). Beyond replication: division and segregation of mitochondrial DNA in
649   kinetoplastids. *Molecular and Biochemical Parasitology*, *196*(1), 53–60.
650   https://doi.org/10.1016/j.molbiopara.2014.03.008

651   Robinson, D. R., Sherwin, T., Ploubidou, A., Byard, E. H., & Gull, K. (1995). Microtubule polarity and
652   dynamics in the control of organelle positioning, segregation, and cytokinesis in the
653   trypanosome cell cycle. *The Journal of Cell Biology*, *128*(6), 1163.
654   https://doi.org/10.1083/JCB.128.6.1163

655   Schaffer, M., Mahamid, J., Engel, B. D., Laugks, T., Baumeister, W., & Plitzko, J. M. (2017). Optimized
656   cryo-focused ion beam sample preparation aimed at in situ structural studies of membrane
657   proteins. *Journal of Structural Biology*, *197*(2), 73–82.
658   https://doi.org/10.1016/J.JSB.2016.07.010

659   Schimanski, B., Aeschlimann, S., Stettler, P., Käser, S., Gala, M. G. F., Bender, J., Warscheid, B., Vögtle,
660   F. N., & Schneider, A. (2022). p166 links membrane and intramitochondrial modules of the
661   trypanosomal tripartite attachment complex. *PLoS Pathogens*, *18*(6).
662   https://doi.org/10.1371/JOURNAL.PPAT.1010207

663   Schnarwiler, F., Niemann, M., Doiron, N., Harsman, A., Kaser, S., Mani, J., Chanfon, A., Dewar, C. E.,
664   Oeljeklaus, S., Jackson, C. B., Pusnik, M., Schmidt, O., Meisinger, C., Hiller, S., Warscheid, B.,

665   Schnaufer, A. C., Ochsenreiter, T., & Schneider, A. (2014). Trypanosomal TAC40 constitutes a
666   novel subclass of mitochondrial B-barrel proteins specialized in mitochondrial genome
667   inheritance. *Proceedings of the National Academy of Sciences*, *111*(21), 7624–7629.
668   https://doi.org/10.1073/pnas.1404854111

669   Schneider, A., & Ochsenreiter, T. (2018). Failure is not an option – mitochondrial genome segregation
670   in trypanosomes. *Journal of Cell Science*, *131*(18), jcs221820.
671   https://doi.org/10.1242/jcs.221820

672   Schneiter, M., Halm, S., Odriozola, A., Mogel, H., Rička, J., Stoffel, M. H., Zuber, B., Frenz, M., &
673   Tschanz, S. A. (2021). Multi-scale alignment of respiratory cilia and its relation to mucociliary
674   function. *Journal of Structural Biology*, *213*(1). https://doi.org/10.1016/J.JSB.2020.107680

675   Schumann Burkard, G., Jutzi, P., & Roditi, I. (2011). Genome-wide RNAi screens in bloodstream form
676   trypanosomes identify drug transporters. *Molecular and Biochemical Parasitology*, *175*(1), 91–
677   94. https://doi.org/10.1016/j.molbiopara.2010.09.002

678   Shi, J., Franklin, J. B., Yelinek, J. T., Ebersberger, I., Warren, G., & He, C. Y. (2008). Centrin4
679   coordinates cell and nuclear division in T. brucei. *Journal of Cell Science*, *121*(Pt 18), 3062–3070.
680   https://doi.org/10.1242/jcs.030643

681   Speichers, D. W., Weglarz, L., & Desilva, T. M. (1992). Properties of Human Red Cell Spectrin
682   Heterodimer (Side-to-Side) Assembly and Identification of an Essential Nucleation Site. *Journal*
683   *of Biological Chemistry*, *267*(21), 14775–14782. https://doi.org/10.1016/S0021-9258(18)42107-
684   2

685   Sun, S. Y., Kaelber, J. T., Chen, M., Dong, X., Nematbakhsh, Y., Shi, J., Dougherty, M., Lim, C. T.,
686   Schmid, M. F., Chiu, W., & He, C. Y. (2018). Flagellum couples cell shape to motility in
687   Trypanosoma brucei. *Proceedings of the National Academy of Sciences of the United States of*
688   *America*, *115*(26), E5916–E5925. https://doi.org/10.1073/pnas.1722618115

689   Trager, W. (1965). The Kinetoplast and Differentiation in Certain Parasitic Protozoa. *The American*
690   *Naturalist*, *99*(907), 255–266. https://doi.org/10.1086/282371

691   Trikin, R., Doiron, N., Hoffmann, A., Haenni, B., Jakob, M., Schnaufer, A., Schimanski, B., Zuber, B., &
692   Ochsenreiter, T. (2016). TAC102 Is a Novel Component of the Mitochondrial Genome
693   Segregation Machinery in Trypanosomes. *PLOS Pathogens*, *12*(5), e1005586.
694   https://doi.org/10.1371/journal.ppat.1005586

695   Tskhovrebova, L., Trinick, J., Sleep, J. A., & Simmons, R. M. (1997). Elasticity and unfolding of single
696   molecules of the giant muscle protein titin. *Letters to Nature*, *387*(15), 308–312.

697   Tyler, K. M., Matthews, K. R., & Gull, K. (2001). Anisomorphic cell division by African trypanosomes.
698   *Protist*, *152*(4), 367–378. https://doi.org/10.1078/1434-4610-00074

699   Vaughan, S., & Gull, K. (2016). Basal body structure and cell cycle-dependent biogenesis in
700   Trypanosoma brucei. *Cilia*, *5*(1), 5. https://doi.org/10.1186/s13630-016-0023-7

701   Wan, W. (2020). *TOMOMAN* (No. 0804020). Zenodo. https://doi.org/10.5281/zenodo.4110737

702   Wirtz, E., Leal, S., Ochatt, C., & Cross, G. A. (1999). A tightly regulated inducible expression system for
703   conditional gene knock-outs and dominant-negative genetics in Trypanosoma brucei. *Molecular*
704   *and Biochemical Parasitology*, *99*(1), 89–101. https://doi.org/10.1016/s0166-6851(99)00002-x

705   Wolff, G., Limpens, R. W. A. L., Zheng, S., Snijder, E. J., Agard, D. A., Koster, A. J., & Bárcena, M.
706   (2019). Mind the gap: Micro-expansion joints drastically decrease the bending of FIB-milled
707   cryo-lamellae. *Journal of Structural Biology*, *208*(3). https://doi.org/10.1016/J.JSB.2019.09.006

708   Zhao, Z., Lindsay, M. E., Roy Chowdhury, A., Robinson, D. R., & Englund, P. T. (2008). p166, a link
709   between the trypanosome mitochondrial DNA and flagellum, mediates genome segregation.
710   *The EMBO Journal*, *27*(1), 143–154. https://doi.org/10.1038/sj.emboj.7601956

711   Zheng, S. Q., Palovcak, E., Armache, J. P., Verba, K. A., Cheng, Y., & Agard, D. A. (2017). MotionCor2 -
712   anisotropic correction of beam-induced motion for improved cryo-electron microscopy. *Nature*
713   *Methods*, *14*(4), 331. https://doi.org/10.1038/NMETH.4193

714
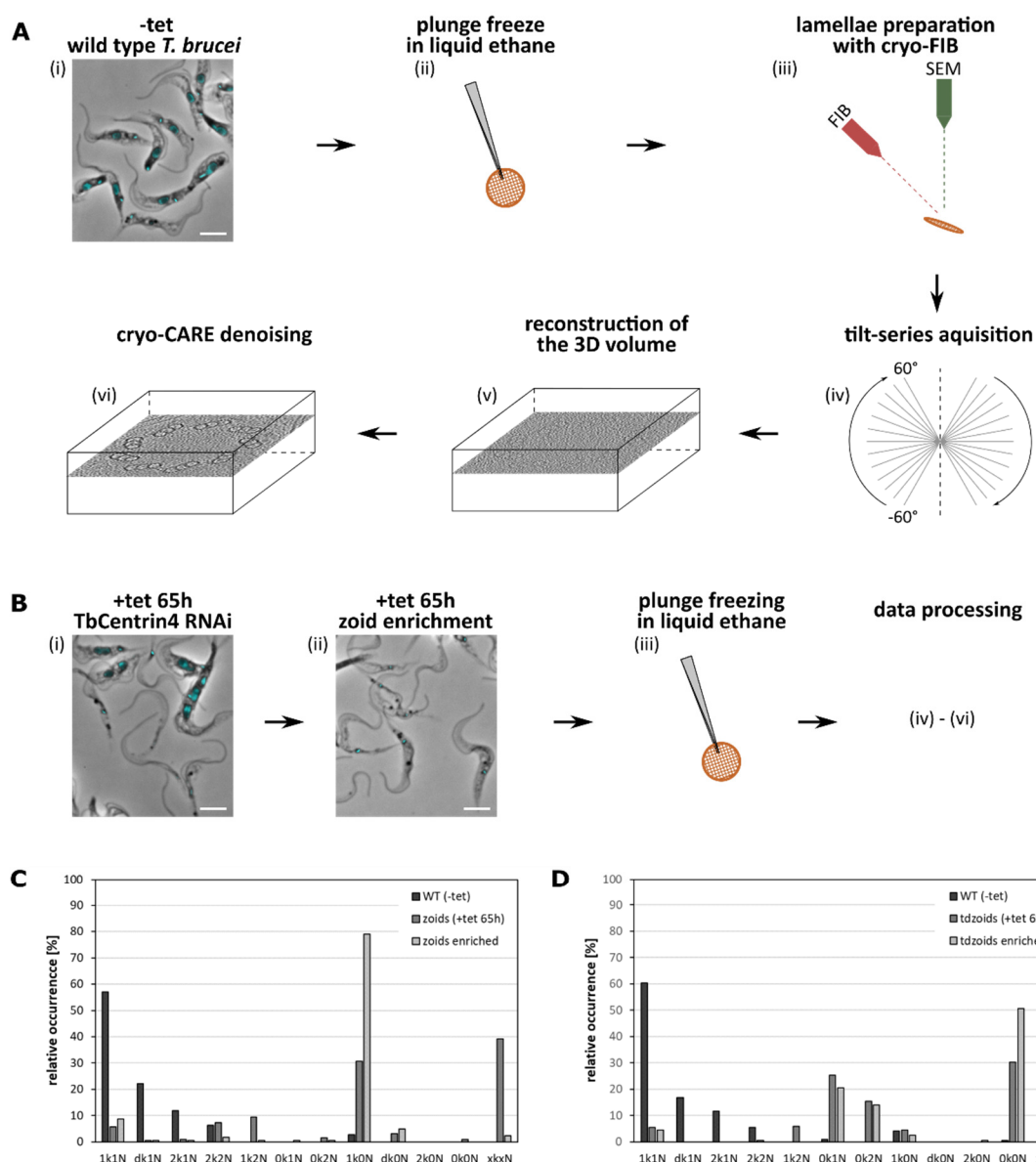
Figures

Figure 1: Overview of the cryo-ET workflow.

A) Schematic overview of the workflow for cryo-FIB milling, cryo-ET and subsequent data processing. (i) Wild type procyclic form trypanosomes are (ii) mounted onto carbon coated copper grids and plunge frozen in liquid ethane. From this point on, the samples are kept at liquid nitrogen temperature at all times. The samples are transferred to an Aquilos 2 scanning electron microscope equipped with a focused ion beam source (FIB) and (iii) lamellae of about 70-200 nm thickness are randomly milled through the trypanosomes. The samples are then transferred to the Titan Krios transmission electron microscope (TEM), where tomographic datasets are collected as (iv) a tilt-series of low dose micrographs. The tilt-series is then (v) preprocessed and reconstructed usin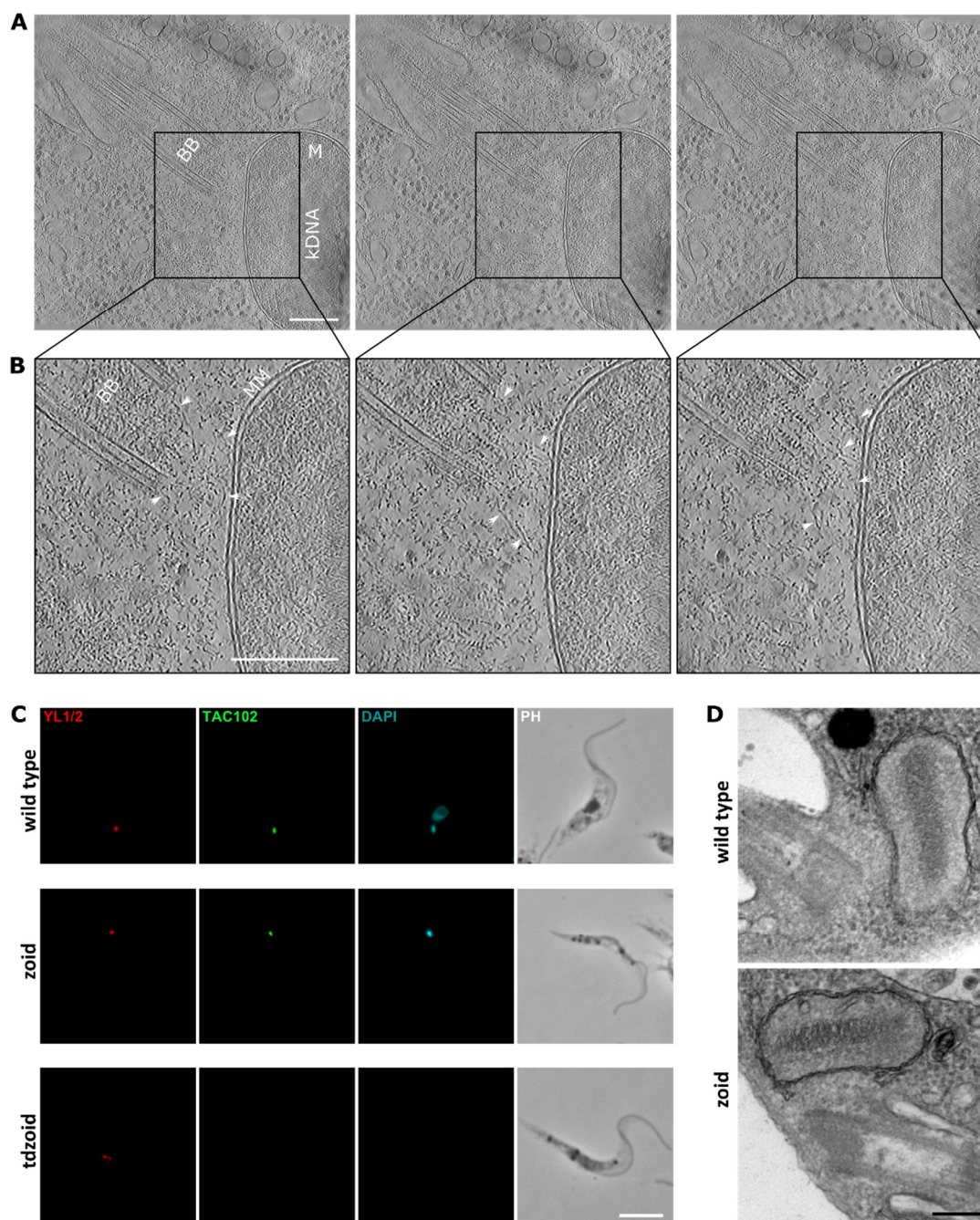g TOMOMAN, MotionCor2 and IMOD, and (vi) denoised with cryo-CARE (Buchholz et al., 2019; Mastronarde & Held, 2017; Wan, 2020; Zheng et al., 2017). The micrograph in (i) shows an overlay of phase contrast with the DNA stain DAPI; scale bar: 5µm. B) Schematic overview of the experimental workflow for cryo-ET of zoids and tdzoids. *T. brucei* cells carrying the TbCentrin4 RNAi (and p197

21

729   RNAi) contruct, are (i) induced for RNAi expression for 65 h hours. The resulting population of

730   trypanosomes (containing about 30 % of zoids) is then harvested, and (ii) enriched for zoids. The zoid

731   fraction is then (iii) transferred to carbon coated copper grids and plunge frozen in liquid ethane.

732   Data acquisition and processing (steps (iv) to (vi)) are identical to the description in A, except for

733   TOMOMAN preprocessing, which was skipped in this case. Micrographs in (i) and (ii) show an overlay

734   of phase contrast with the DNA stain DAPI; scale bar: 5µm. C) Karyotype distributions of wild type *T.*

735   *brucei* (black), TbCentrin4 RNAi cells induced for 65 h (zoids, dark grey) and TbCentrin4 RNAi cells

736   after induction (65 h) and centrifugal enrichment of zoids (zoids enriched, light grey). n ≥ 150. D)

737   Karyotype distributions of wild type *T. brucei* (black), TbCentrin4 p197 double RNAi cells induced for

738   65 h (tdzoids, dark grey) and TbCentrin4 p197 double RNAi cells after induction (65 h) and centrifugal

739   enrichment of tdzoids (tdzoids enriched, light grey). n ≥ 150.

Figure 2: cryo-FIB milling of wild type *T. brucei* and zoid generation by TbCentrin4 RNAi are two alternative approaches for TAC imaging by cryo-ET.

A) Micrographs showing three tomographic z-slices through the TAC region of a wild type *T. brucei* cell. Basal body (BB), mitochondrial kDNA pocket (M) and kDNA are labelled in the images on the left. Scale bar: 200 nm. Full tomogram shown in Movie S 1. B) Magnified images of the exclusion zone. Filamentous structures protrude from the proximal end of the BB towards the mitochondrial membranes (MM). Some well-resolved filaments are marked with arrowheads. Scale bar: 100 nm. C) Immunofluorescence analysis of wild type trypanosomes (top row), zoids (middle) and tdzoids (bottom). The cells were stained with the BB marker YL1/2, that stains for tyrosinated tubulins at the BB, with monoclonal anti-TAC102 antibody and with the DNA stain DAPI. Scale bar: 5 µm. D) TEM

750   analysis of the TAC region in chemically fixed, resin-embedded wild type trypanosomes (top) and

751   zoids (bottom). Scale bar: 250 nm.
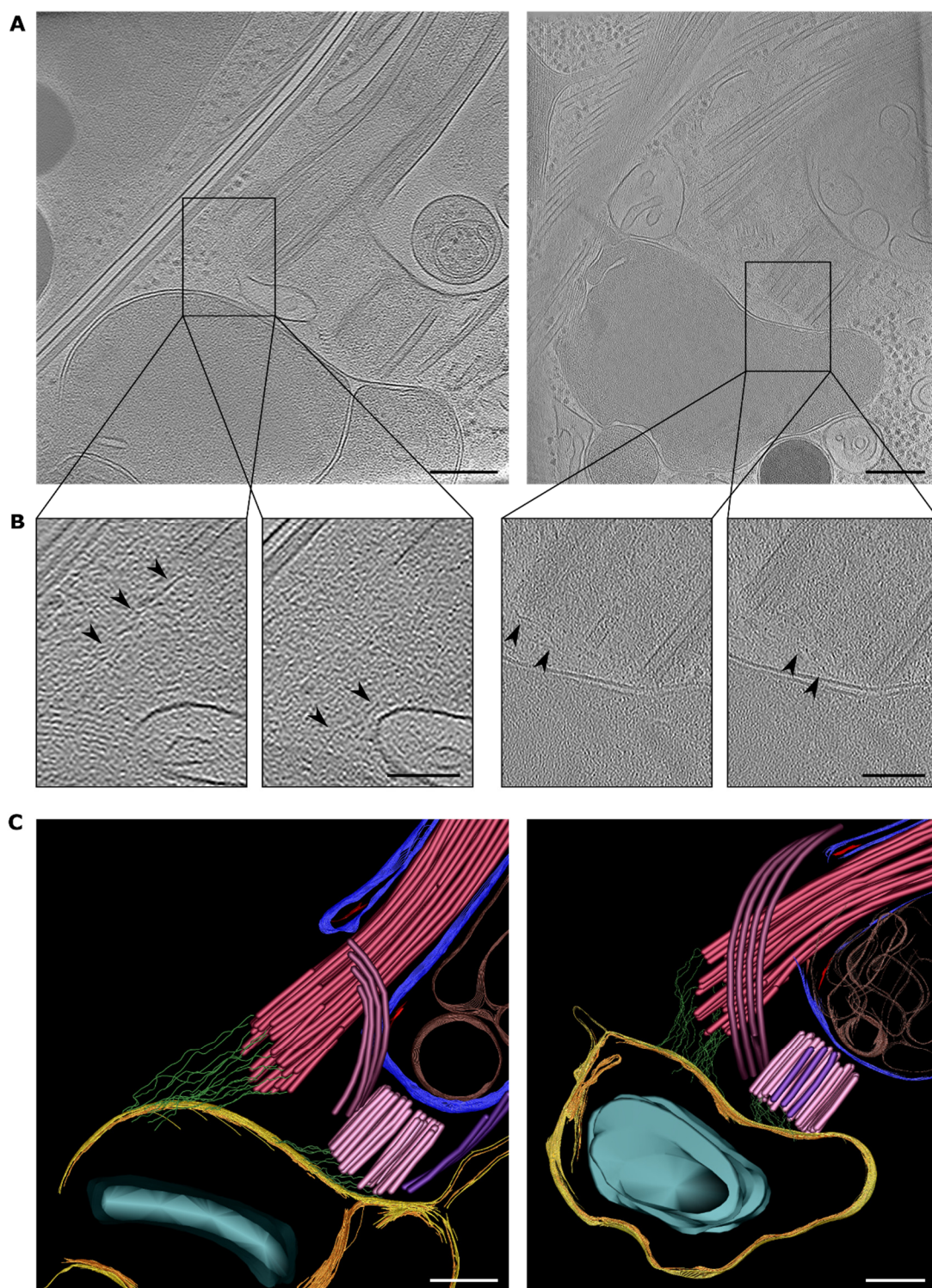
Figure 3: Phenotypical overview and segmentation of the TAC area of zoid *T. brucei* as observed in situ by cryo-ET.

A) Section (maximum intensity projection of 20 slices) through two typical cryo-electron tomograms. Scale bars: 200 nm. Full tomograms shown in Movies S 2 and S 3. B) zoom-in into the exclusion zone, highlighting individual EZFs (maximum intensity projection of 10 slices; arrowheads pointing at the most well-resolved filament in the respective image). Scale bars: 100 nm. C) Model of the TAC area based on segmentations of the tomograms shown in A. BB and flagellum (magenta), pBB (pink), microtubule quartet of the mature BB (purple), growing microtubule quartet of the pBB (violet),

760   flagellar pocket (blue), flagellar pocket vesicles (brown), collarette (red), exclusion zone filaments of

761   the TAC (green), outer mitochondrial membrane (yellow), inner mitochondrial membrane (orange)

762   and kDNA (cyan) have been segmented in cryo-CARE (Buchholz et al., 2019) denoised tomograms.

763   Scale bars: 200 nm. Animations in Movies S 4 and S 5.
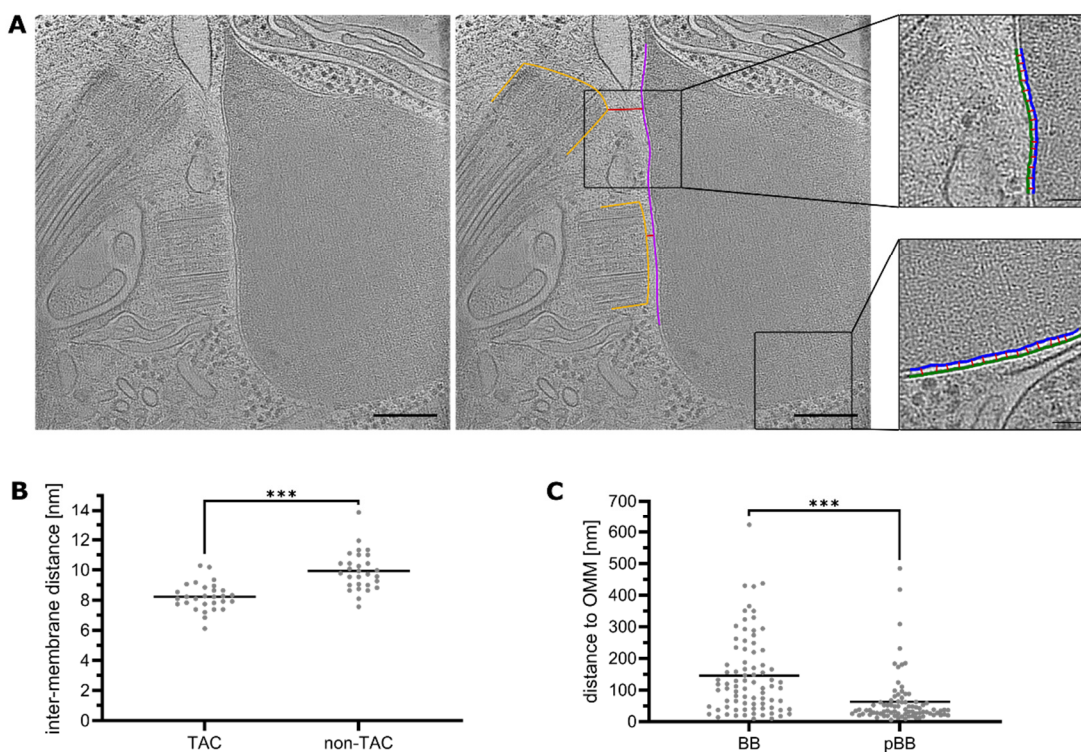
Figure 4: Dimensions of the exclusion zone and the differentiated membranes as observed in cryo-ET.

A) Overview of the measured dimensions in a representative tomogram. (left) single z-slice of a representative tomogram of the TAC area of a *T. brucei* zoid cell; (middle) demonstration of the measurement strategy applied for (C), with the orange line outlining the proximal part of the BB/pBB, pink following the outer mitochondrial membrane (OMM) and red showing the measured distances for BB and pBB distance to the OMM; (right) zoom-in at two membrane patches, one within the TAC area (top) and one outside the TAC area (bottom), blue and green showing inner and outer mitochondrial membrane (IMM and OMM) , red indicating the measured distances (center of the OMM to center of the IMM). Scale bars: 200 nm / 50 nm. Full tomogram shown in Movie S 6. B) Depiction of the results from measurements of the inter-membrane distance of the mitochondrial membranes in the TAC area versus the membrane area outside of the TAC (non-TAC) (measurements from 29 cells, with 15 averaged measurements per membrane patch). Asterisks (*** ≙ p ≤ 0.001) indicate significance of the difference in intermembrane distance. p-value (two-sided t-test) = $5 \cdot 10^{-10}$. C) Collective display of distance measurements obtained from 82 cells. Asterisks (*** ≙ p ≤ 0.001) indicate that the pBB is positioned significantly closer to the OMM than the mature BB is. p-value (two-sided t-test) = $1.4 \cdot 10^{-6}$.
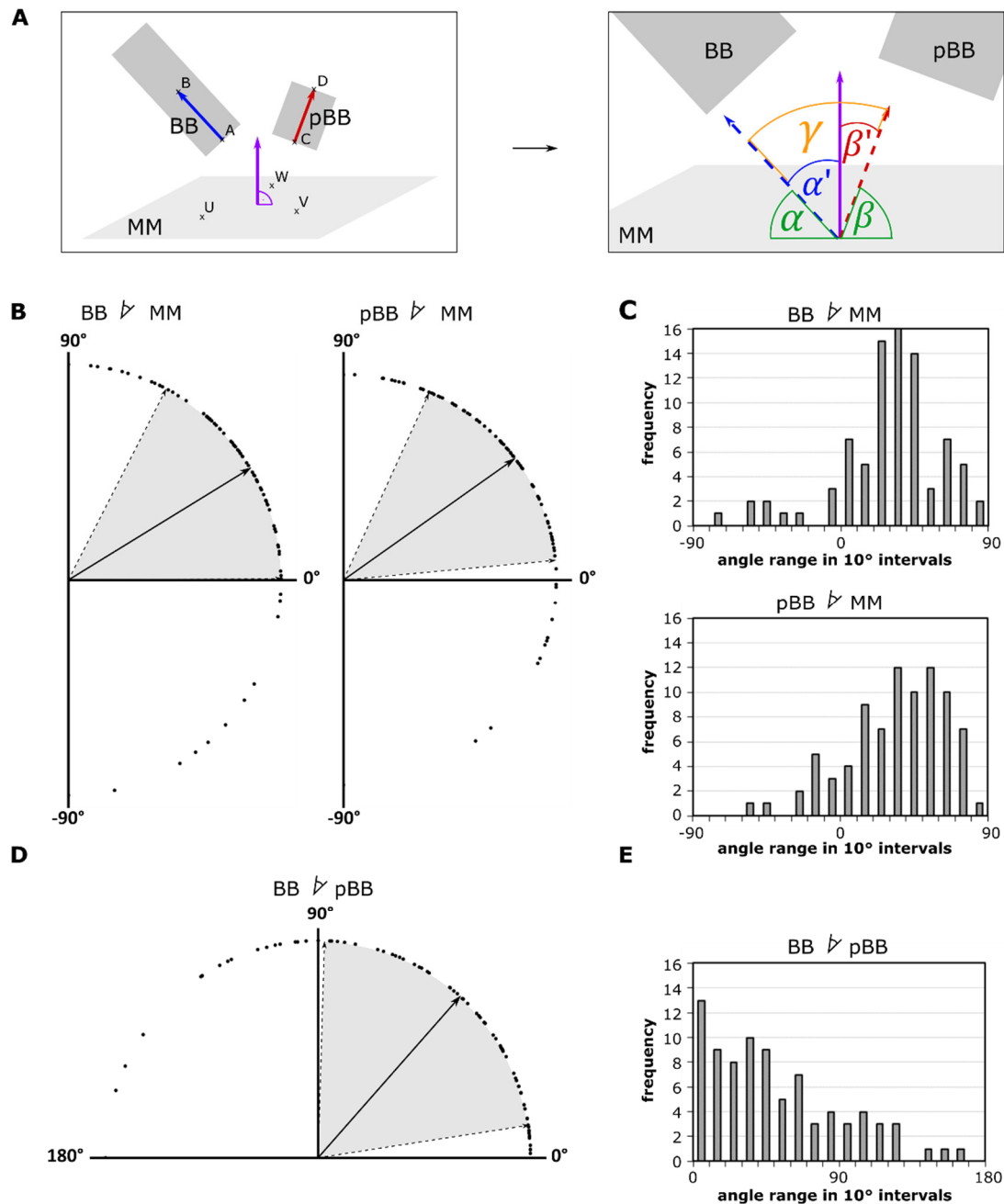
Figure 5: The exclusion zone filaments are highly flexible and allow a wide range of movement for the basal body and pro-basal body.

A) In 3D space we selected three points on the outer mitochondrial membranes (MM; points U, V, W), and two points along the axis of the BB (blue, points A, B) or pBB (red, points C, D). We calculated the angles between the resulting vectors $\overrightarrow{AB}$ and $\overrightarrow{CD}$ for the BB (blue, α') or pBB (red, β') respectively, and the normal vector on the plane built by U, V and W (purple). From these angles, we deduced the angles between vectors $\overrightarrow{AB}$ (green, α) or $\overrightarrow{CD}$ (green, β) and the plane itself. To obtain the vector between BB and pBB, we calculated the angle between $\overrightarrow{AB}$ and $\overrightarrow{CD}$ (orange, γ). B) Visualization of the angles measured between the BB and the MM (left), or the pBB and the MM (right). The membrane plane was selected to be in the area of the TAC, irrespective of the position of any other parts of the MM. The X-axis of each graph represents an angle of 0° between the two structures in question, while points hitting the Y-axis are at a 90°/-90° angle to the MM. The mean angles of 31.6° (BB-MM)

28

793   or 35.4° (pBB-MM) as well as the standard deviations of 31.3° (BB-MM) or 30.1° (pBB-MM) are

794   marked with arrows. The respective standard directional range is shown in grey. C) Histograms

795   illustrating the distribution of the data points shown in B (bin size = 10°). D) Visualization of the angle

796   between BB and pBB. The data is plotted equivalent to B with the mean angle of 48.5° and the

797   standard deviation of 39.8° indicated as described before. E) Histogram illustrating the distribution of

798   the data points shown in D (bin size = 10°).
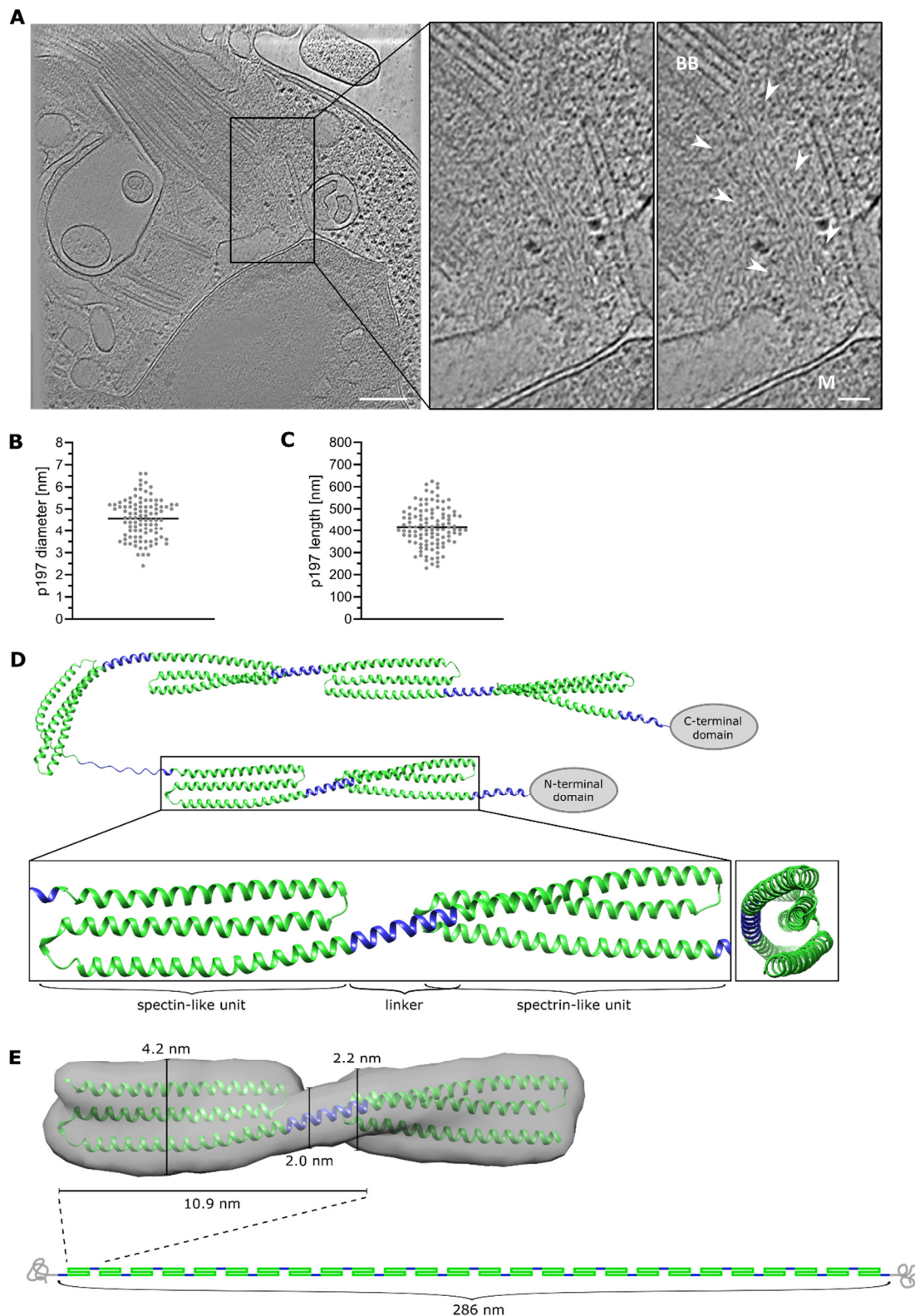
799 Figure 6: Structural analysis of individual p197 filaments.

800 A) Exemplary image of the p197 filaments as observed in cryo-electron tomograms. Overview of the

801 TAC area on the left (scale bar: 200 nm) and a magnified view of the exclusion zone in the middle.

802 The picture on the right shows the same zoom-in, with additional annotations: M, mitochondrion;

803 BB, basal body; scale bar: 50 nm. Arrowheads point at the region where p197 is clearly visible. Full

804 tomogram shown in Movie S 7; zoom-in of the EZF shown in Movie S 8. B) Summary of

805   measurements on filament diameter collected from a total of ten tomograms with ten

806   measurements per tomogram. C) Summary of measurements of filament length collected on a total

807   of 22 tomograms with five measurements per tomogram. Individual filaments were traced manually,

808   by following them across the 3D volume. D) Structure of the repeat section of p197 (six repeats) as

809   predicted by AlphaFold2 (top panel, (Jumper et al., 2021)). Repetitive coiled coil structures (spectrin-

810   like units) are depicted in green, while linker regions are shown in blue. The N- and C-terminal

811   domain are represented schematically, as these areas of the protein were poorly resolved in the

812   prediction. A subset of two spectrin-like units connected with the typical α-helical linker are shown

813   and labelled in the bottom panel. The panel on the bottom right shows the top view onto the same

814   subsection of the protein. E) (top) modelled substructure of two spectrin-like units in a density map

815   of 1.5 nm resolution. Model diameters were measured and to range from 2.2 – 4.2 nm in the

816   spectrin-like unit and down to 2 nm in the linker region. Based on the model, filament rise per

817   spectrin-like unit plus linker is 10.9 nm. (bottom) schematic representation of full length p197,

818   consisting of 26 spectrin-like units that are interspaced by the α-helical linker. The repetitive stretch

819   is connected to the N- and C-terminal domains with the same α-helical linker. Total predicted length

820   of the modelled protein domain is 286 nm.
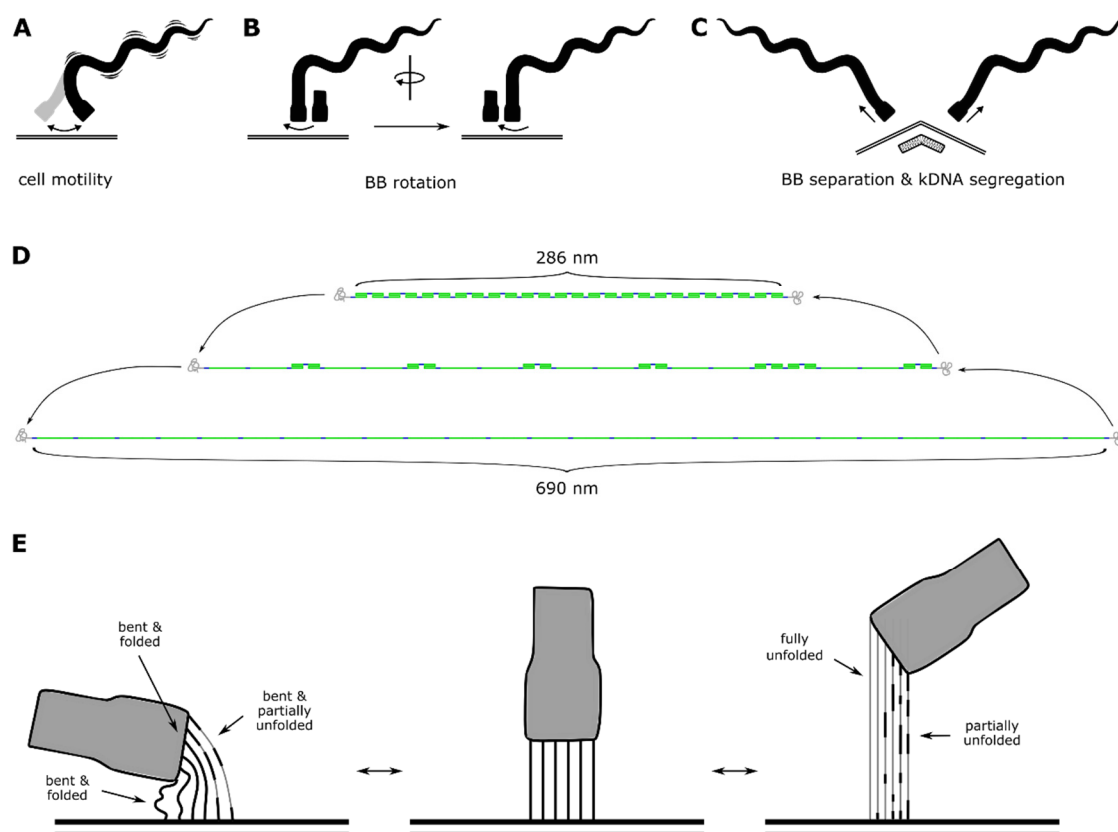
Figure 7: Cell motility and cell cycle dynamics impose mechanical forces on p197 that result in the reversible unfolding of spectrin-like units.

A) – C) Sources of BB/pBB movement relative to the OMM. The EZFs must withstand these movements. A) Being the base of a motile flagellum, the mature BB is subject to slight but constant tumbling movements. B) The freshly matured BB has been shown to rotate around its maternal BB to relocate to a position posterior of the maternal BB (Vaughan & Gull, 2016). C) kDNA segregation depends on the separation of the BBs prior to cytokinesis (Ogbadoyi et al., 2003). A stable connection between the BBs and the kDNA is essential for kDNA segregation. D) The effects described in A) – C) impose varying levels of mechanical force on p197. Individual p197 molecules will release spectrin-like units from their coiled coil assembly to account for BB/pBB movements. Upon rapprochement of the BB/pBB to the OMM, the tension is reduced, allowing spectrin-like units to fold back into the relaxed, coiled coil conformation. In its extremes, the repeat section extends from 286 nm (relaxed state) to a maximum of 690 nm (fully extended state). E) Overview of different positional arrangements of the BB towards the mitochondrial membranes. p197 responds to the varying distance between the BB and the OMM by bending and (un)folding in respect to the level of mechanical force imposed to the individual filament.

837   Supplementary Figures
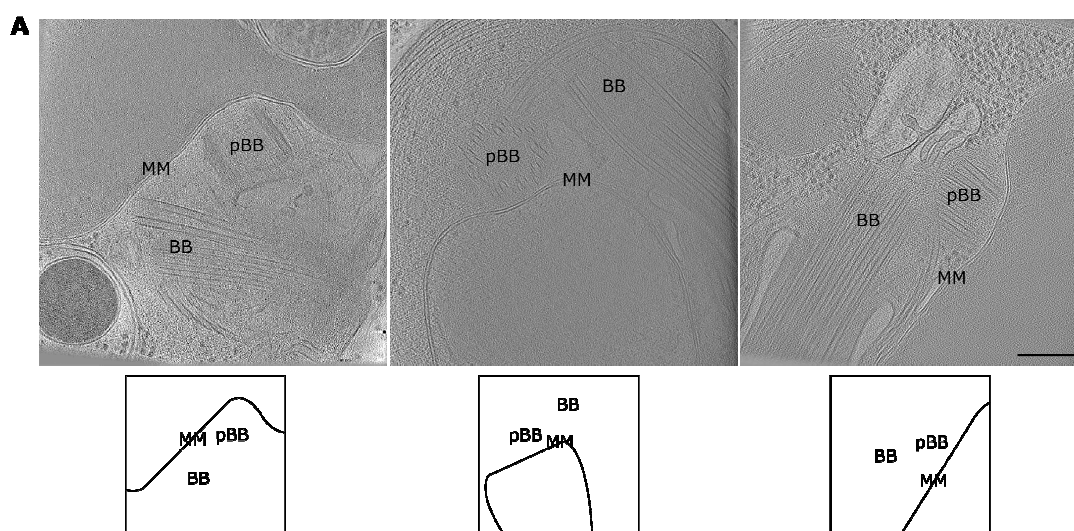
838   Figure S 1: The EFZ allow for a wide range of orientations of the basal bodies with

839   respect to the mitochondrial membranes

840   A) (top) Representative tomographic slices demonstrating the diversity of orientations observed

841   among the relevant structures (bottom). For visualization purposes, schematic representations of the

842   basal body (BB), pro-basal body (pBB) and the mitochondrial membranes (MM) are depicted on the

843   bottom of each tomographic slice.
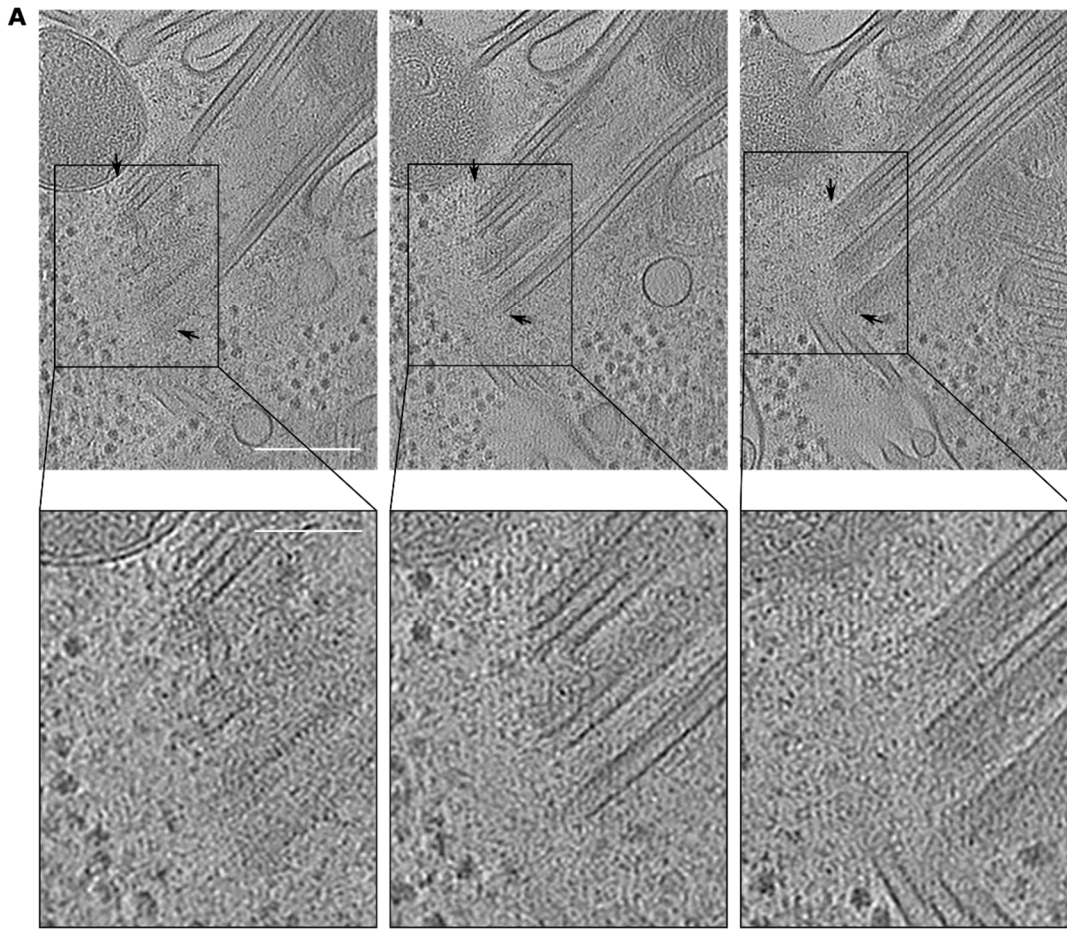
844   Figure S 2: tdzoids do not contain any EZFs.

845   A) To verify that the filaments we describe as EZFs are indeed part of the TAC, we performed cryo-ET

846   on Tbcentrin4 p197 double RNAi cells (tdzoids). These cells are depleted of p197 and therefore also

847   lack any downstream TAC components. The tomographic images depicted in the top row each show

848   a 10-slice maximum intensity projection of a tomogram denoised with cryo-CARE (Buchholz et al.,

849   2019). The image stacks are taken at three different heights along the cross-section of the mature BB

850   (increasing z-height from left to right). Arrows point at the proximal face of the BB, where we the

851   EZFs emanate in regular zoids. Scale bar: 200 nm. The bottom row shows zoom-ins at the region

852   proximal to the BB. Scale bar: 100 nm.
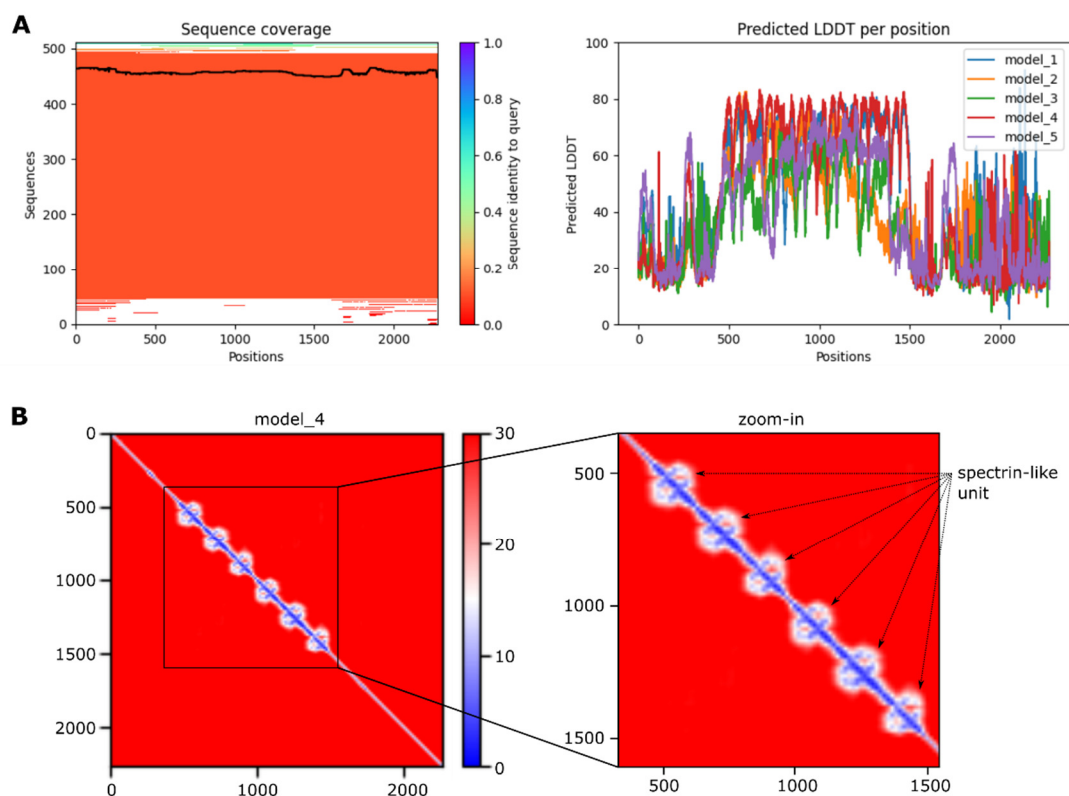
Figure S 3: Predictive scores of the AlphaFold2 prediction of the shortened p197-6Rep sequence.

A) Sequence coverage and local distance difference test (LDDT) plot of the AlphaFold2 (Jumper et al., 2021) run of a shortened version of p197 consisting of the N-terminal domain, six repeats and the C-terminal domain. Model_4 was selected for further analysis, as it scores highest in LDDT of the repeat section of the protein. B) Predicted aligned error (PAE) plot of the full sequence prediction (left) and zoom-in into the repeat section of model_4.

A N-terminal domain | rep1 | rep2 | rep3 | rep4 | rep5 | rep6 | rep7 | C-terminal domain

B
```
MSGLTSHNISATSIRVHGITRERDMCVFCRKRSSPPPNDPLAPVFAFFSLVDCRHYACQPCALVHCDNAGRHIRCPACC
AISRLAQSGRRRGNRVDERVPIDDGVSSAASQSSKRVLAPPKRSLSVTDRRRRTSSVQFSTNLTSPSGQKEALSTGGSN
TSLTLAAVGRLPTDPNYSKGKGDEGGTVAAFSEEERISVDLYTIKGTAAKRPRRTTAERARSQPLPPAEYRYLPPPTPF
HRPPPLVIHTIEEEEEVAASFQLIVREIEQTIAATLVKEADERDTIGIAEAHRRNVLSKLREEDERKRFAAHHELNDEF
SDAKLSPRTTTNASDGQVSETSDEGMSELSTQQDSIQKNYKQPIDQKAMITKERTGTPTAAEKQTKHQQQTITKQNTEE
EKKEAKNENNKESKKKRRERVEVATWDSEQQLRLFEQLMDLARDEQQHRAKIQRDETRMHAEMERSEASDVATIKAAME
AMAESARREQEELLRDEKEERYTIQEDERRLRRNITRQSAELSLDVSMQHVQQRGKEDAQRELDMLRVALESTAVETTS
RARLNLIVTEELRARDSLCSDEASERAMHAAEERRERVEVATWDSEQQLRLFEQLMDLARDEQQHRAKIQRDETRMHAE
MERSEASDVATIKAAMEAMAESARREQEELLRDEKEERYTIQEDERRLRRNITRQSAELSLDVSMQHVQQRGKEDAQRE
LDMLRVALESTAVETTSRARLNLIVTEELRARDSLCSDEASERAMHAAEERRERVEVATWDSEQQLRLFEQLMDLARDE
QQHRAKIQRDETRMHAEMERSEASDVATIKAAMEAMAESARREQEELLRDEKEERYTIQEDERRLRRNITRQSAELSLD
VSMQHVQQRGKEDAQRELDMLRVALESTAVETTSRARLNLIVTEELRARDSLCSDEASERAMHAAEERRERVEVATWDS
EQQLRLFEQLMDLARDEQQHRAKIQRDETRMHAEMERSEASDVATIKAAMEAMAESARREQEELLRDEKEERYTIQEDE
RRLRRNITRQSAELSLDVSMQHVQQRGKEDAQRELDMLRVALESTAVETTSRARLNLIVTEELRARDSLCSDEASERAM
HAAEERRERVEVATWDSEQQLRLFEQLMDLARDEQQHRAKIQRDETRMHAEMERSEASDVATIKAAMEAMAESARREQE
ELLRDEKEERYTIQEDERRLRRNITRQSAELSLDVSMQHVQQRGKEDAQRELDMLRVALESTAVETTSRARLNLIVTEE
LRARDSLCSDEASERAMHAAEERRERVEVATWDSEQQLRLFEQLMDLARDEQQHRAKIQRDETRMHAEMERSEASDVAT
IKAAMEAMAESARREQEELLRDEKEERYTIQEDERRLRRNITRQSAELSLDVSMQHVQQRGKEDAQRELDMLRVALEST
AVETTSRARLNLIVTEELRARDSLCSDEASERAMHAAEERRERVEVATWDSEQQLRLFEQLMDLARDEQQHRAKIQRDE
TRMHAEMERSEADGILACGAQSEGADSFEVASSGCDCVFRPSGADCASFSPYVCRGGGVLPLDVEIPVGLAYSAHGSTS
AEVISVDYTSFLPIVGSDAQGESSLWNTLDDDGGVVFGDVCAGGDDVGIDVNDVESVHISRGCSTVLDAGGVGATAEVY
ALDEKWRDGTAVSAEPPRIPASRICRTCFSTDTSRCARCGTMVCSHCIPSGSFRQCCTLHHLTIINKRCRVMTETRVHA
RWECRRLFRQFRLEQRMRRRRENVVNTRGFDVVVLTPEQKGDNSNLHEVKTPPRVTRRFLNQENDSEEDAAWKSHYLES
WPSDSGQMPPCGLKQERFDEFNDAENSMNLTADNEPKTERKRATAFFVPLGNSAEPRRPKPPTPRNYVPGIIHNCTKAP
QSKRAVSRMRFRRLRRQNATGNTKNTTLNSAAAGRNVQEHRAASSSKPRPQESWARQRPVQRQGAFITADPVRGITRSG
PTSNSWRRRNFRTKSRSPAGYGGKASACNFHGDRCGDAMALGRTYYDGNPVRSKGLAYVLDEEPPQRGYEPTPPTRLQS
NRVVKSGVHSGEEHTRMGCQHEWEPDQQCVPLFEEFHASSSTPPWRPPFSRDPPPPRRNHRNTNIGGRTHRTLAPFPAR
QRLCHPRQRSAADLTRNASPGQACSRFHYNPLDDVDRAAFVGGPRGAQRQPPTSVAEPCITVHLFPPSSYGGGAGTSGR
HPLRGPTARRHSSRAHRPSPARAASPPWRTDLNTPFICPPWNANRPDTFIAKPYTRTTCRR
```

Figure S 4: Sequence composition of the truncated version of p197 as used for modelling.

A) schematic overview of the construct analysed AlphaFold2. N- and C-terminal domain are depicted in grey; sequence repeats 1 – 6 (rep1 – rep7) are shown in red, orange, green, cyan, blue, purple and pink. Repeat 7 is an incomplete repeat consisting of the first 53 amino acids of the sequence of repeats 1 – 6. B) sequence of the construct analysed in AlphaFold2. Colors match the colors in A.

Supplementary Movies

867

868   Movie S 1: Overview of the cryo-electron tomogram shown in Figure 2 A. Scale bar: 100 nm.

869   Movie S 2: Overview of the cryo-electron tomogram shown in Figure 3 A (left). Scale bar: 100 nm.

870   Movie S 3: Overview of the cryo-electron tomogram shown in Figure 3 A (right). Scale bar: 100 nm.

871   Movie S 4: Animation of the model shown in Figure 3 C (left). Scale bar: 200 nm.

872   Movie S 5: Animation of the model shown in Figure 3 C (left). Scale bar: 200 nm.

873   Movie S 6: Overview of the cryo-electron tomogram shown in Figure 4 A. Scale bar: 200 nm.

874   Movie S 7: Overview of the cryo-electron tomogram shown in Figure 6 A. Scale bar: 100 nm.

875   Movie S 8: zoom-in of the exclusion zone of the cell shown in the cryo-electron tomogram in Figure 6
876   A. Scale bar: 50 nm.